Engineering Fracture Mechanics 176 (2017) 186–212

Contents lists available at ScienceDirect

Engineering Fracture Mechanics

journal homepage: www.elsevier.com/locate/engfracmech

Dynamic mixed-mode fracture behaviors of PMMA and polycarbonate

Balamurugan M. Sundaram, Hareesh V. Tippur *

Department of Mechanical Engineering, Auburn University, AL 36849, United States

ARTICLE INFO

Article history:
Received 4 December 2016
Received in revised form 27 February 2017
Accepted 28 February 2017
Available online 6 March 2017

Keywords:
Dynamic fracture
Mixed-mode crack initiation
Material characterization
Fracture envelope
Optical measurements
Transparent materials

ABSTRACT

Mixed-mode dynamic crack initiation and growth in polymethymethacrylate (PMMA) and polycarbonate (PC) are studied experimentally. A simple specimen geometry in conjunction with a dynamic loading configuration to generate different mode-mixities at crack initiation is demonstrated. A Hopkinson pressure bar is used to rapidly load free-standing edge cracked samples in a reverse impact configuration. By eccentrically loading the specimen relative to the crack line, various mode-mixities at crack initiation are achieved by increasing the initial crack length while keeping all other experimental parameters the same. A relatively new full-field optical technique, Digital Gradient Sensing (DGS), along with high-speed photography is used to perform full-field measurements. DGS measures instantaneous angular deflections of light rays representing two orthogonal stress gradients under plane stress conditions. The mode-I and -II stress intensity factor histories are evaluated via over-deterministic least-squares analysis of optically measured data. By quantifying the critical stress intensity factors evaluated at crack initiation, dynamic fracture envelopes are developed for both the polymers. The results are studied comparatively and relative to the brittle fracture criteria. From measured stress intensity factors and crack speeds in the post-initiation regime, energy release rate vs. velocity plots for different mixed-mode configurations are produced for both the polymers.

1. Introduction

Different yet complementary factors have motivated this research. They include a need for (a) characterizing mixed-mode dynamic fracture behavior of transparent armor materials [1], (b) extending a commonly used loading geometry to generate a range of mode-mixities at dynamic crack initiation, (c) extending a relatively new full-field optical methodology to visualize and quantify dynamic mixed-mode crack initiation and growth parameters in ductile and brittle polymers.

Dynamic mixed-mode cracking is rather common when engineering materials and structures experience a combination of tensile and shear tractions. Despite many years of research on dynamic fracture mechanics, crack initiation under mixed-mode conditions is not fully understood [1–4]. Of interest to this research are mixed-mode fracture behaviors of transparent polymethylmethacrylate (PMMA) and polycarbonate (PC) used widely in engineering practice for their optical transparency, stiffness, and resistance to cracking but are not studied extensively under mixed-mode dynamic loading conditions common in safety structures and armor systems [5]. These two polymers show many similarities in their physical and mechanical characteristics (density, elastic modulus, yield strength) except ductility; PC exhibits significant ductility [6] relative to

* Corresponding author.
E-mail address: tippuhv@auburn.edu (H.V. Tippur).

http://dx.doi.org/10.1016/j.engfracmech.2017.02.029
0013-7944/

PMMA (100% vs. 2–3% strain at failure under static conditions) and hence would be of interest to study their mixed-mode fracture performance comparatively under rapid loading conditions.

Most reported works on dynamic mixed-mode fracture use global measurements and/or complementary computational simulations to recover fracture parameters such as crack initiation toughness and kink angles. However, this necessitates approximations while interpreting the measured data. Alternatively, a few investigators use optical methods such as photoelasticity [7], caustics [1], Coherent Gradient Sensing (CGS) [8,9] and Digital Image Correlation (DIC) [10] in conjunction with high-speed photography for visualizing and quantifying dynamic fracture behavior as full-field local measurement methods are generally preferred to global measurement techniques. With the introduction of DIC methods, the requirements such as material birefringence for performing photoelasticity, complications due to *K*-dominance requirements in caustics, and challenges with laser interferometry setups in CGS seem to call for better full-field optical methods to investigate fracture mechanics. In this context, a full-field white light optical method called Digital Gradient Sensing (DGS) [11,12] that uses speckle correlation and provides full-field information in the digital form seems to be an attractive alternative. Other advantages such as easily variable measurement sensitivity, amenability to ultrahigh-speed photography, simultaneous measurement of two orthogonal field quantities, availability of measured data as rectangular arrays for easy post-processing, absence of a need for creating speckles on samples, and applicability to study both transparent and opaque solids, all add to its appropriateness for dynamic fracture mechanics investigation. Further, the availability of orthogonal stress gradients in the entire field makes it feasible to obtain stresses via post-processing [13].

Although there are reports in the literature on different loading configurations and geometries for characterizing crack initiation and growth under dynamic mode-I conditions, the same for mixed-mode counterparts is limited. Broadly, previous works have used eccentrically loaded 3-point bend edge notched beams [8], centrally notched Brazilian disks subjected to compression [14] or other geometries to generate dominant mode-I or mode-II loading separately. Brazilian disk configuration can produce a wide range mode-mixities but the presence of dual crack-tips is experimentally challenging in terms of initiating cracks simultaneously. In light of this, a simpler specimen geometry capable of producing a wider if not the entire range of mode-mixities is desirable.

In the following, the rationale and description of the proposed specimen geometry to generate different mode-mixities is presented first. This is followed by sections on optical measurement of mixed-mode crack-tip fields using transmission-mode DGS in conjunction with high-speed photography. The extraction of crack-tip parameters from optical measurements at different mode-mixities to generate crack initiation envelopes for PMMA and PC follows next. Discussion of results and conclusions of the work are reported at the end of the article.

2. Methodology to vary mode-mixities under stress wave loading

A specimen configuration involving a reverse impact loading of a single edge notched (SEN) geometry capable of producing a range of mode-mixities is proposed. The specimen geometry and loading configuration is shown schematically in Fig. 1.

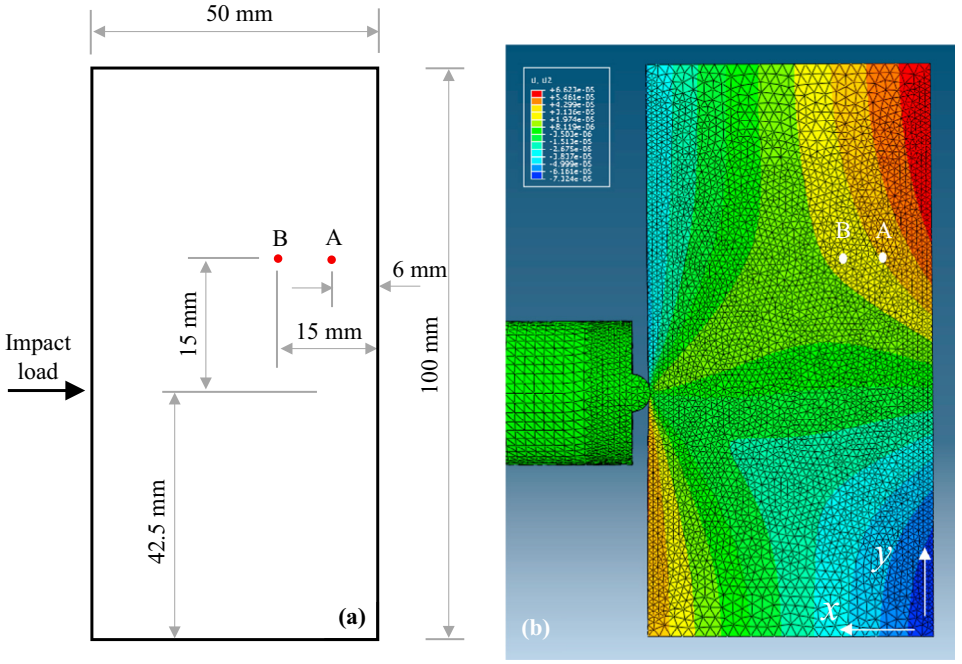

Fig. 1. (a) Specimen configuration used. (b) Discretized finite element model with an overlay of displacement contours in the *y*-direction from numerical simulation at an arbitrary time instant during impact (striker velocity ~ 13.5 m/s).

To understand the rationale and help arrive at this specimen/loading configuration, numerical simulations were performed first. Elasto-dynamic finite element simulations were carried out on the specimen geometry using ABAQUS®/Explicit software platform. A Hopkinson pressure bar setup loading an edge of a free standing cracked plate was modeled. The impact end of the long-bar was shaped into a half-cylinder to produce a line-load on the specimen edge. The specimen and the long-bar were discretized into 259,337 and 37,952 solid 3D tetrahedral elements, respectively. Plane stress with the corresponding specimen thickness was imposed on the cracked specimen during simulations. The discretized model overlaid with displacement contours in the y-direction is shown in Fig. 1(b). Two points of interest A and B on the specimen were identified, as shown in Fig. 1, to monitor stress fields during the impact loading event. (These points correspond to two prospective crack-tip locations in the proposed specimen geometry.) The time steps during the elasto-dynamic analysis were allowed to be automatically controlled by the explicit integration scheme. The elastic modulus and Poison's ratio of PMMA, obtained from an ultrasonic pulse-echo measurement of longitudinal and shear wave speeds [15], and its mass density were used in the simulations. The long-bar was modeled using the elastic properties of AL-7075 used in the experiments, to be detailed later. Tables 1 and 2 list the material properties of PMMA and the AL-7075 aluminum long-bar, respectively. The particle velocity ($V_p(t) = C\varepsilon(t)$ where C is the bar wave speed) history, obtained from a measured strain gauge history ($\varepsilon(t)$) on the long-bar during an actual experiment (to be detailed later), was used as an input for numerical simulations. The normal stress (σ_{yy}) and in-plane shear stress (σ_{xy}) at points A (distance of A from the edge a = 6 mm; a/w = 0.12 from the free edge, w being the width of the plate = 50 mm) and B (distance of B from the edge a = 15 mm; a/w = 0.3 from the free edge) were monitored during the course of the loading event and are shown in Fig. 2(a) and (b), respectively. It can be seen that σ_{yy} at both the points are compressive between 15 and 45 μs ($0.8 < \frac{t}{t^*} < 2.4$ where $t^* = w/C_L$ represents excursion time for the longitudinal wave over the width of the sample and C_L the longitudinal wave speed of PMMA (~2750 m/s) as the impact induced waves travel initially from the near edge towards the far edge. The reflected tensile waves from the free edge cause a tensile stress beyond $\frac{t}{t^*} \sim 2.4$. During this time interval, at Point A σ_{yy} increases rapidly when compared the one at point B. On the other hand, at the corresponding time instants, the magnitude of σ_{xy} increases rapidly at point B when compared to the one at point A. In the $0.8 < \frac{t}{t^*} < 2.4$ interval, shear stresses at these points are significantly larger than the corresponding σ_{yy}. In light of these, if the tip of a horizontal edge crack originating at the far (right) edge of the plate were at point A, it will experience a lower shear to tensile stress ratio (σ_{xy}/σ_{yy}) and hence a lower mode-mixity than a prospective crack-tip at point B. Thus, by increasing the crack length from 6 mm (Point A) to 15 mm (Point B), one could potentially increase the mode-mixity at crack initiation when all other parameters are same.

Another potential method for altering the mode-mixity at crack initiation in the reverse impact geometry is to vary the impact velocity between experiments while maintaining all other experimental parameters and the specimen geometry the same. That is, when the impact velocity is increased in the specimen configuration (Fig. 1), the normal and shear stress histories at the prospective crack-tip location (say, point B) change. The shear stresses increase and normal stresses are lower until a certain time (~50 μs or $\frac{t}{t^*} > 2.4$ in this case). This increases the shear to tensile stress ratio at the point of interest. Hence, if a crack-tip were present at B, it would attain lower mode-I and higher mode-II stress intensity factors earlier due to the higher impact velocity and initiate at a different mode-mixity if initiation conditions are reached. This is demonstrated in Fig. 3(a) and (b) where σ_{yy} and σ_{xy} histories, respectively, for two different impact velocities (13.5 m/s and 16 m/s) are plotted at location B (see, Fig. 1). The argument is further supported by multiple experiments using a SEN specimen geometry with crack-tip at point B (a = 15 mm; e = 15 mm) subjected to impact velocities ranging from 10.5 m/s to 19 m/s. The crack initiated and kinked at significantly higher angles, from 32.6 deg. to 62.2 deg (as shown in Fig. 4(a)–(e)), as the

Table 1
Some properties of long-bar used.

Dynamic properties of AL-7075 long-bar	
Parameter	Value
Density	2730 kg/m^3
Elastic modulus	71.7 GPa
Poisson's ratio	0.30
Longitudinal wave speed in bar	5700 m/s

Table 2
Some properties of cast PMMA used [16].

Dynamic properties of PMMA	
Parameter	Value
Density	1010 kg/m^3
Elastic modulus	5.3 GPa
Poisson's ratio	0.34
Elasto-optic constant	-1.08×10^{-10} m^2/N

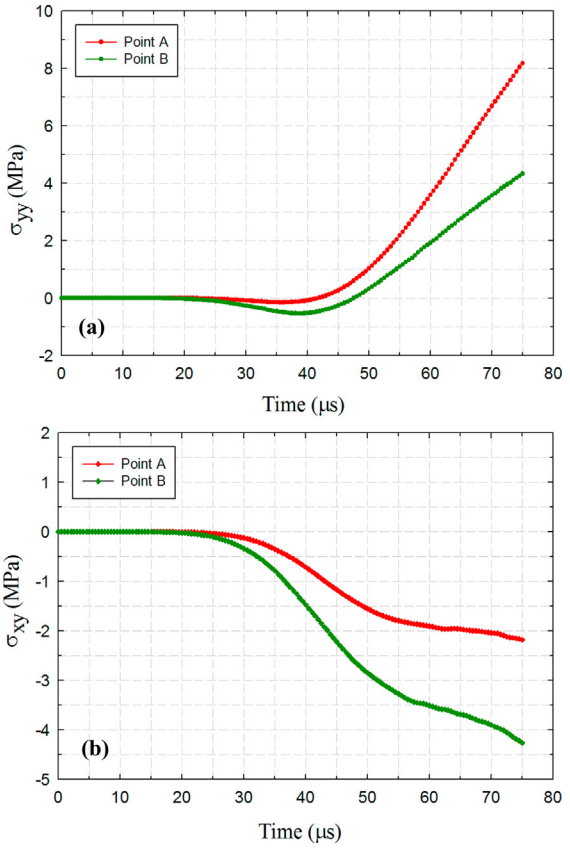

Fig. 2. Stress field evolution at Points A and B of an uncracked specimen (see, Fig. 1) subjected to eccentric impact loading (striker velocity ~ 13.5 m/s).

impact velocity was increased. However, *the former method of increasing the crack length is chosen for the current investigation to avoid potential loading rate effects at different velocities contaminating mixed-mode crack initiation behavior*.

3. Digital Gradient Sensing (DGS)

A schematic of the experimental setup for transmission-mode DGS technique is shown in Fig. 5. In this technique [17] a random speckle pattern on a planar surface, called a 'speckle target,' is photographed through a planar, optically transparent specimen being monitored. Ordinary white light illumination is used to record random gray scales on the target. The speckle pattern is first photographed through the specimen in its undeformed state to obtain a reference image. That is, a point P on the target plane (x_0-y_0 plane) is recorded by the camera through point O on the specimen plane (x-y plane). Upon loading, the non-uniform state of stress alters the refractive index of the specimen in the crack-tip vicinity. Additionally, the Poisson effect produces non-uniform thickness changes. A combination of these, called the *elasto-optic effect*, causes the light rays to deflect from their original path as they propagate in the crack-tip vicinity. The speckle pattern is once again photographed through the specimen in the deformed state. Now, the point P appears to have shifted to Q when recorded by the camera through point O on the specimen after deformation. The local deviations of light rays can be quantified by correlating speckle images in the deformed and reference states to obtain speckle displacements in the x- and y-directions, δ_x and δ_y, respectively. Once displacements δ_x and δ_y are evaluated from digital image correlation, the angular deflections of light rays ϕ_x and ϕ_y in two orthogonal planes x-z and y-z planes, the z-axis coinciding with the optical axis of the setup and x-y being the specimen plane coordinates, can be computed knowing the distance between the specimen plane and the target plane. A detailed paraxial analysis by Periasamy and Tippur [11] shows that the local angular deflections are related to the gradients of the in-plane normal stresses as,

$$\phi_{x;y} = \pm C_\sigma B \frac{\partial(\sigma_{xx} + \sigma_{yy})}{\partial x; y} \tag{1}$$

where C_σ is the elasto-optical constant of the specimen material, B is its initial thickness and σ_{xx} and σ_{yy} denote the thickness-wise averages.

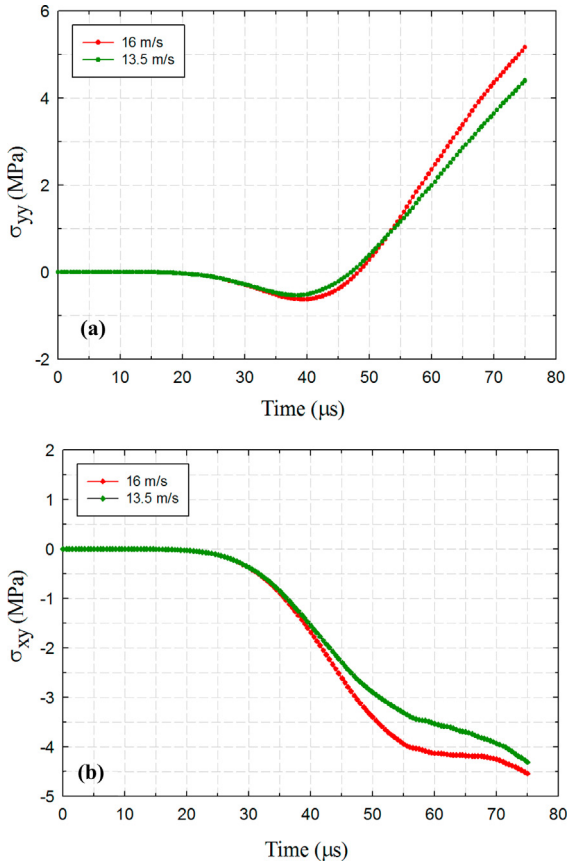

Fig. 3. Stress field evolution at Point B for different impact velocities (striker velocity ~ 13.5 m/s and 16 m/s) on an uncracked specimen.

4. Mixed-mode fracture of PMMA

4.1. Specimen preparation and geometry

SEN plate specimens of PMMA were prepared to carry out dynamic fracture experiments. The specimens of 100 mm × 50 mm × 8.6 mm were cut from cast PMMA sheets (see Fig. 6). An initial notch was machined into the specimen using a 300 μm thick diamond impregnated saw. The notch length (and location of the notch tip) was varied to obtain different mode-mixities (see inset in Fig. 6 for details) while the eccentricity (e) between the loading point on the opposite face and the crack location was kept constant. Five different configurations were used to produce various mode-mixities at crack initiation. This included the mode-I case with an eccentricity $e = 0$. The initial notch tip in each case was sharpened using a razor blade and the resulting sharpness of the tip is as shown in the inset of Fig. 6. Evidently, the resulting crack-tip root radius is at least an order of magnitude lower than the initial notch radius.

4.2. Experimental setup

The dynamic mixed-mode fracture of PMMA specimens were studied using transmission-mode DGS in conjunction with ultrahigh-speed digital photography. The schematic of the experimental setup used is shown in Fig. 7. A Hopkinson pressure bar (long-bar) was used for loading the single edge pre-notched specimen. It was a 1.83 m long-bar of 25.4 mm diameter with a cylindrical end (line-load) pressed against an unconstrained PMMA plate on the edge opposite to the cracked edge (see, Fig. 8). The sample was positioned on the platform of a micro-positioning stage using a 2 mm thick strip of soft putty between the specimen and the platform. Another identical putty strip was placed on the top edge of the specimen to ensure symmetry in terms of acoustic impedance. A 305 mm long, 25.4 mm diameter rod held in the barrel of a gas-gun was co-axially aligned with the long-bar and was used as the striker. Both the long-bar and the striker were made of AL 7075-T6 eliminating any impedance mismatch between them during impact. A striker velocity of 13.5 ± 0.5 m/s was employed uniformly in all tests and the corresponding strain history measured off the

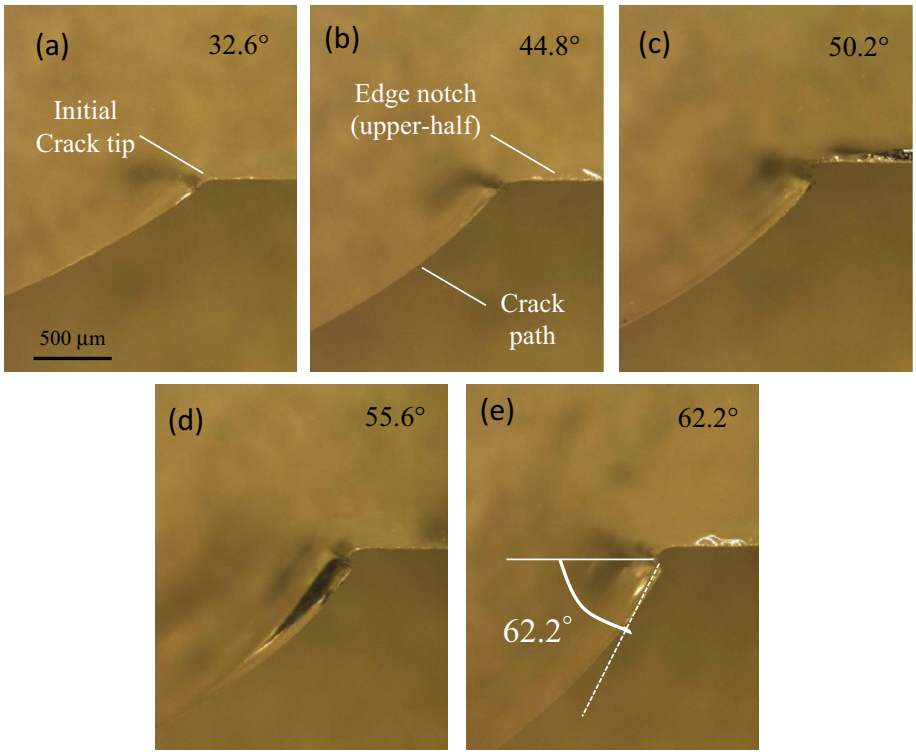

Fig. 4. Close up images of crack initiation in PMMA specimens (a = 15 mm; e = 15 mm) at various impact velocities of (a) 10.5 m/s, (b) 12 m/s, (c) 13.5 m/s, (d) 16 m/s, (e) 19 m/s. The crack initiation angle relative to the initial notch orientation is shown on the right top corner of each photograph of the upper-half of the fractured specimen.

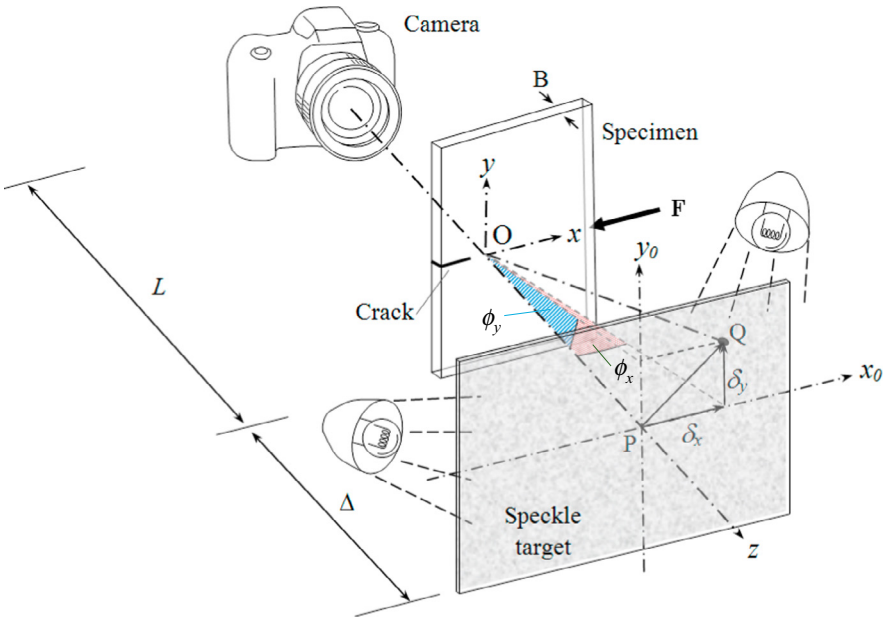

Fig. 5. The schematic of the experimental setup for transmission-mode Digital Gradient Sensing (DGS) technique to determine stress gradients in transparent sheets.

long-bar was used to obtain the particle velocity that was input into the finite element simulations. A separate experiment was carried out with the high-speed camera focused on the striker impacting the long-bar to measure the impact velocity.

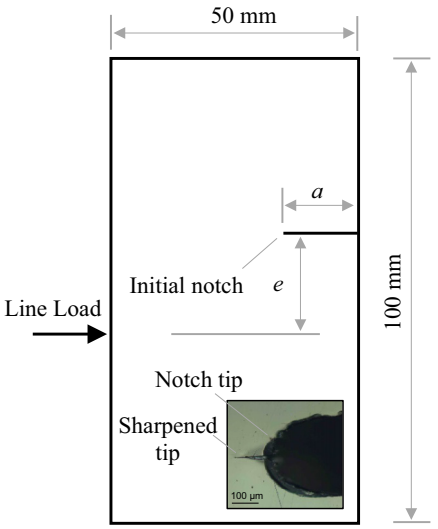

Mode-I	Config.1	$a = 6$ mm, $e = 0$ mm
Mixed-mode	Config.2	$a = 6$ mm, $e = 15$ mm
	Config.3	$a = 9$ mm, $e = 15$ mm
	Config.4	$a = 12$ mm, $e = 15$ mm
	Config.5	$a = 15$ mm, $e = 15$ mm

Fig. 6. Specimen configuration used in mixed-mode dynamic fracture experiments. Values of a and e used are listed in the table. Inset shows the initial notch tip (PMMA) sharpened using a razor blade. (The line-load and the initial crack are equidistant relative to the horizontal axis of the specimen.)

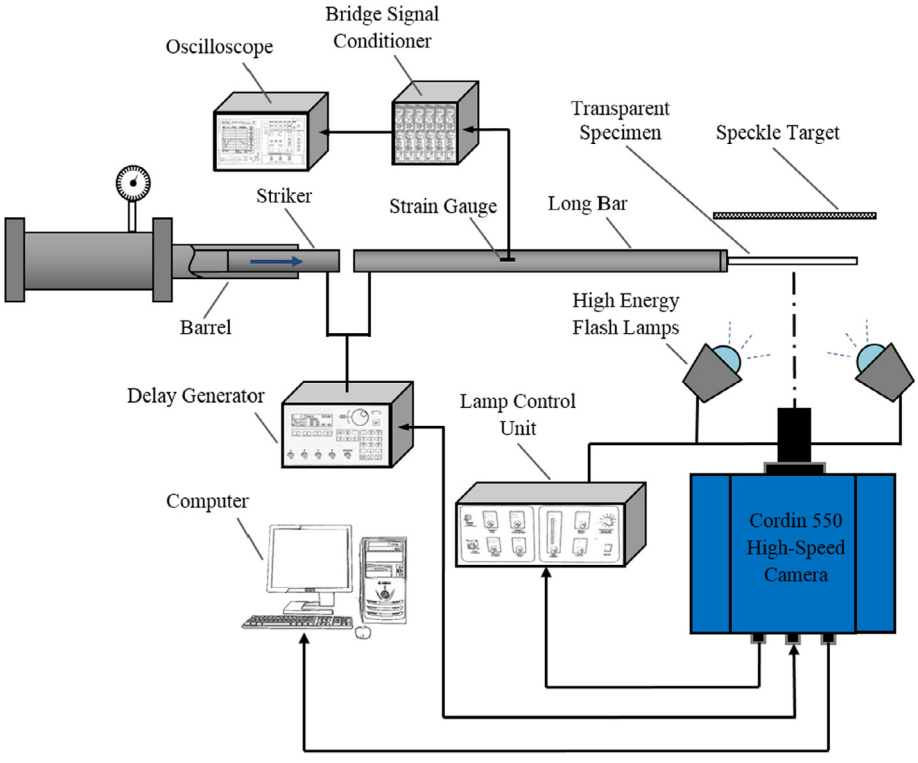

Fig. 7. Experimental setup used for dynamic mixed-mode fracture.

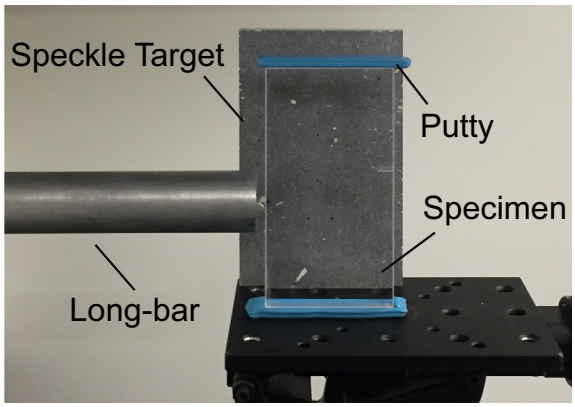

Fig. 8. Close-up view of the specimen loading configuration used in mixed-mode fracture experiments.

The speckle images were acquired using a Cordin-550 ultrahigh-speed digital camera with 32 CCD sensors of 1000 × 1000 pixels spatial resolution and 8 bit grayscale resolution positioned radially around a five-facet rotating mirror. The imaging system also included two high-energy flash lamps producing broad-band white light illumination needed to capture the speckles decorating the target plane. Experimental parameters such as the trigger delay, flash duration, framing rate, CCD gain, and data storage were controlled using a computer connected to the camera. A 28–300 mm focal length macro zoom lens mounted on an adjustable bellows was used for imaging. Further, the lens aperture was kept open as widely as possible (numerical aperture on the lens was F#5.6) to achieve a good exposure with minimum electronic gain setting during photography. The specimen was at a distance of approximately 850 mm in front of the camera. A speckled target plate was placed behind the specimen at a distance (Δ) of 29.3 mm from the mid-plane of the specimen. A pair of heavy dots (Fig. 9) was marked on the target plate to help relate the dimension on the image to the actual specimen/target dimensions during image analysis. The speckles covered approximately 4–5 pixels; or, the scale factors ranged between 22 and 24 pixels/mm.

The region of interest in this study was in the neighborhood of the initial notch tip. That is, the camera recorded approx. 45 mm × 45 mm region. Prior to loading the specimen, a set of 32 speckle images were recorded in the undeformed state at 400,000 frames per second. Enough care was exercised to achieve a near Gaussian distribution of gray scales for each speckle image, typically in the mid-range of 0–255 gray scale by optimizing the position of the flash lamps. Next, without altering any of the camera settings, the striker was launched towards the long-bar. When the striker contacted the long-bar, a compressive stress wave was set-off in the long-bar, which propagated over its length before compressively loading the crack-free specimen edge. The *loading phase* of the stress pulse generated was ~120 μs. As the striker contacted the long-bar, a trigger signal was generated prompting the camera to record a second set of 32 images at the same framing rate as the specimen was loaded by stress waves. A trigger delay was used to adjust the recording window due to the fixed number of frames (32) of the camera. Thus, a total of 32 pairs of images in the deformed and undeformed (reference) states were recorded at 2.5 μs intervals between successive images. Two such speckle images in the region of interest, one in the undeformed state and the other in deformed state with a kinked dynamically growing crack, are shown in Fig. 9. The corresponding two images from each sensor were paired (from the undeformed and deformed) sets and correlated separately.

4.3. Image analysis and evaluation of crack-tip parameters

The 2D digital image correlation was carried out using the image correlation software ARAMIS®. Each image was segmented into facets/sub-images consisting of 25 × 25 pixels. An overlap of 20 pixels (i.e., step size of 5 pixels) was used during image analysis. This resulted in 194 × 194 matrix of data points in the region of interest for each of the two orthogonal speckle displacement fields. The corresponding angular deflections of light rays were subsequently determined using the known distance (Δ) between the specimen and the target planes.

The position of the crack-tip in each digitized image was used to measure the instantaneous crack length. The crack extension data typically includes measurement errors. To minimize the errors, a quadratic Bézier curve [18,19] was fitted to the crack length data at a time instant '*i*' as,

$$a_i(s) = (1-s)^2\hat{a}_i + 2s(1-s)\hat{a}_{i+1} + s^2\hat{a}_{i+2}, \quad 0 \leqslant s \leqslant 1 \tag{2}$$

where s, $\hat{a}$ and a are the smoothing parameter, the digitized crack length, and the smoothed crack length, respectively. In the above expression $\hat{a}_i, \hat{a}_{i+1}, \hat{a}_{i+2}$ are the control points of $a_i(s)$. The value of s was 0.5 such that the smoothed data point is at the middle of the interval. Subsequently, the crack velocity (V) was estimated from the smoothed crack length history using backward difference method,

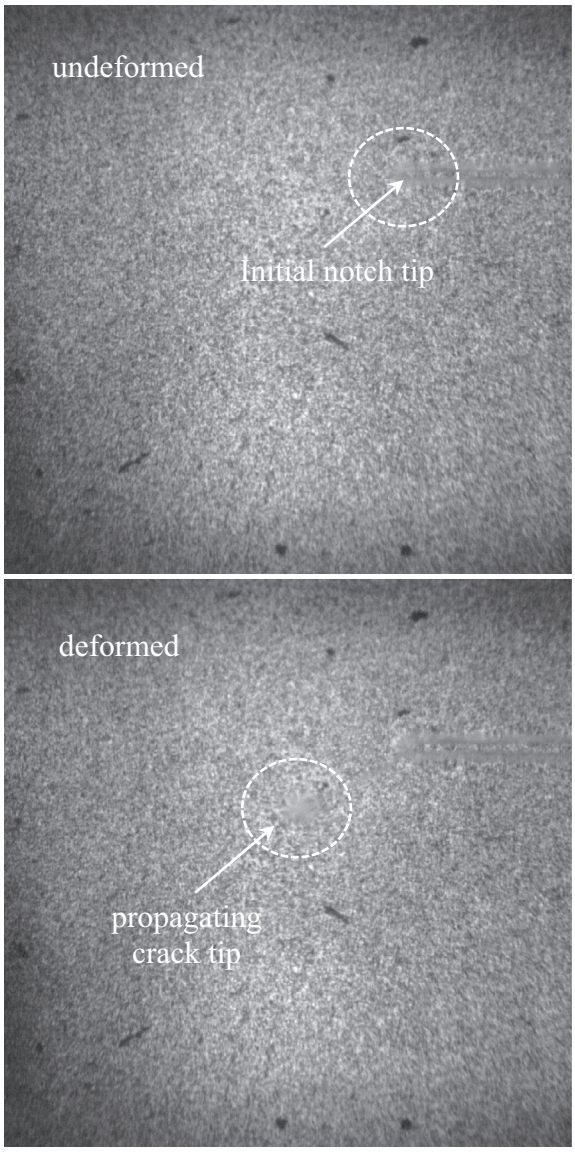

Fig. 9. Speckle images in the undeformed (top) and deformed (bottom) states recorded by the high-speed camera though a PMMA specimen.

$$V_i = \frac{a_i - a_{i-1}}{t_i - t_{i-1}} \tag{3}$$

where a and t are crack length and time, respectively.

Using the two orthogonal angular deflection fields in the x- and y-directions, the instantaneous counterparts in the local coordinates (x', y') (x' coincided with the local crack growth direction) for a moving crack were obtained via coordinate transformation. The mode-I and mode-II stress intensity factors were evaluated from an over-deterministic least-squares analysis of the crack-tip data in conjunction with the asymptotic equation (see [16,20] for details),

$$\phi_{x'}(t) = \phi_x(t)\cos\theta(t) + \phi_y(t)\sin\theta(t) = C_\sigma B\left[-\frac{1}{2}r_l^{-\frac{3}{2}}\left\{f(V;C_L;C_S)A_1(t)cos\left(\frac{3\theta_l}{2}\right) + g(V;C_L;C_S)D_1(t)\sin\left(-\frac{3\theta_l}{2}\right)\right\}\right.$$
$$\left. + \sum_{N=2}^{\infty}\left\{A_N(t)\left(\frac{N}{2}-1\right)r_l^{\left(\frac{N}{2}-2\right)}cos\left((\frac{N}{2}-2)\theta_l\right) + D_N(t)\left(\frac{N}{2}-1\right)r_l^{\left(\frac{N}{2}-2\right)}\sin\left(\left(\frac{N}{2}-2\right)\theta_l\right)\right\}\right] \tag{4}$$

where f and g are functions of instantaneous crack velocity, and (r_l, θ_l) denote the contracted crack-tip polar coordinates, C_σ is the elasto-optical constant of the material, and B is its initial thickness. Further, (r_l, θ_l) can be expressed in the local Cartesian coordinates (x', y') as, $r_l = \{(x')^2 + \alpha_L^2(y')^2\}^{1/2}$ and $\theta_l = \tan^{-1}(\frac{\alpha_L y'}{x'})$. The coefficients of $A_1(t)$ and $D_1(t)$ in the asymptotic

series are related to the mode-I and mode-II stress intensity factors $K_I(t)$ and $K_{II}(t)$, respectively, as $A_1(t) = K_I(t)\sqrt{2/\pi}$ and $D_1(t) = K_{II}(t)\sqrt{2/\pi}$. The functions f and g are,

$$f(V;C_L,C_S) = \left(\frac{1+v}{1-v}\right)\frac{(1+\alpha_S^2)(1-\alpha_L^2)}{4\alpha_L\alpha_S-(1+\alpha_S^2)^2} \text{ and } g(V;C_L,C_S) = \left(\frac{1+v}{1-v}\right)\frac{2\alpha_S(1-\alpha_L^2)}{4\alpha_L\alpha_S-(1+\alpha_S^2)^2} \tag{5}$$

where $\alpha_L = \left[1-\frac{\rho(1-v)}{2\mu}V^2\right]^{\frac{1}{2}}$ and $\alpha_S = [1-\frac{\rho}{\mu}V^2]^{\frac{1}{2}}$ for plane stress. Here, μ and ρ are shear modulus and mass density, respectively. Data in the region ($0.35 < r/B < 0.85$) and ($-135° < \theta < 135°$) near the crack-tip with $N = 4$ was used during analysis. Further, Eqs. (4) and (5) can be reduced to the form of a dynamically loaded stationary crack in the limit the crack velocity $V \to 0$. From the fractured samples, the kink angles at crack initiation were measured for various configurations and compared with the ones predicted by the Maximum Tensile Stress (MTS) criterion [21] that the crack growth occurs normal to the direction of maximum hoop stress. Thus the crack kink angle predicted by the MTS criterion can be expressed as,

$$\alpha_{kink} = \cos^{-1}\left(\frac{3K_{II-cr}^2 \pm \sqrt{K_{I-cr}^4 + 8K_{I-cr}^2K_{II-cr}^2}}{K_{I-cr}^2 + 9K_{II-cr}^2}\right) \tag{6}$$

where $K_{I\text{-}cr}$ and $K_{II\text{-}cr}$ are critical mode -I and mode-II stress intensity factors *at crack initiation*, respectively.

4.4. Experimental results

4.4.1. Crack-tip deformations, crack initiation and growth

Photographs of five fractured samples from each of the configurations are shown in Fig. 10(a)–(e). The stress wave loading occurred on the left edge of the specimen evident as a crater (whitened region) near the impact point. In these images, the crack initiates from the initial tip (near the right edge) and propagates towards the left edge as indicated by the arrowhead. In each case the path the crack took was different. In Fig. 10(a) the crack propagated self-similarly until it reached the free edge and deviated from its initial path due to a loss of in-plane constraint. In Fig. 10(b)–(e) the crack propagated in mixed-mode with a distinct kink at initiation in each case. Fig. 10(a1)–(e1) show the close-up view in the initial crack-tip vicinity and the corresponding kink angles. The crack initiation angle monotonically increased from 'config. 1' to 'config. 5' (0°, 24.8°, 36.2°, 41.4°, 52.3°). This clearly shows that the mode-mixity increased with crack length when eccentricity was constant. The crack initiation angles predicted by the MTS criterion was also evaluated and are listed in Table 3. Both of them show good agreement.

Plots of measured angular deflection contours ϕ_x and ϕ_y proportional to stress gradients $(\sigma_{xx}+\sigma_{yy})_{,x}$ and $(\sigma_{xx}+\sigma_{yy})_{,y}$ (the comma notation denotes derivatives with respect to the subscript) obtained from the image correlation for two select configurations namely, 'config. 1' and 'config. 5' are shown in Figs. 11 and 12, respectively. Further, note that the plots presented are only for two select time instants (one at crack initiation and another during propagation) for brevity. (The contour levels and the scale bar are shown in the first plot in each set and are applicable to the other plots as well.) In these, $t = 0$ μs represents the time the crack initiated at the original tip. In each figure, top and bottom rows correspond to ϕ_x and ϕ_y, respectively. Fig. 11 shows angular deflection contours for config. 1 ($a = 6$ mm; $e = 0$ mm). The crack followed nearly a straight path during the window of observation. It can be seen that the relative size of the contours increased during propagation suggesting an increase in stress intensity factors during the observation window. Further, as expected, the crack-tip contours representing the stress gradients $(\sigma_{xx}+\sigma_{yy})_{,x}$ are approximately symmetric relative to the initial crack whereas $(\sigma_{xx}+\sigma_{yy})_{,y}$ contours are clearly antisymmetric. The (partially visible) contours near the left edge of the region-of-interest are caused by the concentrated line-load acting on the sample. Fig. 12 shows the angular deflection contours for config. 5 ($a = 15$ mm; $e = 15$ mm). The measured contours of $(\sigma_{xx}+\sigma_{yy})_{,x}$ and $(\sigma_{xx}+\sigma_{yy})_{,y}$ are both asymmetric throughout the loading history. The crack initiated at an angle relative to its initial orientation. At time $t = 0$ μs the angular deflection contours are rotated relative to the initial notch and are oriented towards the direction of crack initiation. Further, the number of contours increased with time during the observation window implying an increase in the stress intensity factors.

4.4.2. Crack velocity and stress intensity factor histories

A compilation of crack velocity histories for all the configurations are shown in Fig. 13(a). In all configurations, the crack rapidly accelerates for about 10 μs after initiation followed by a more gradual increase in velocity. At the end of the window of observation, which is $t = 25$ μs, the final velocity monotonically increased from 267 m/s in config. 1 to 347 m/s in config. 5. This suggests that the crack tends to travel faster under higher mixed-mode conditions.

Representative stress intensity factor histories for config. 1 and config. 5 are presented in Fig. 14(a) and (b), respectively. The time axis is shifted such that $t = 0$ corresponds to the instant at which the crack initiated at the initial tip. In case of config. 1 (see Fig. 14(a)) the mode-I stress intensity factor monotonically increase in the pre-initiation period and continues to do so in the post-initiation period as well. Mode-II stress intensity factor remains very low throughout as expected for a mode-I crack. Nevertheless, mode-II stress intensity factor should be ideally zero and the deviations provide an estimate of errors associated with the stress intensity factor extraction method based on least-squares analysis of optical data. In case

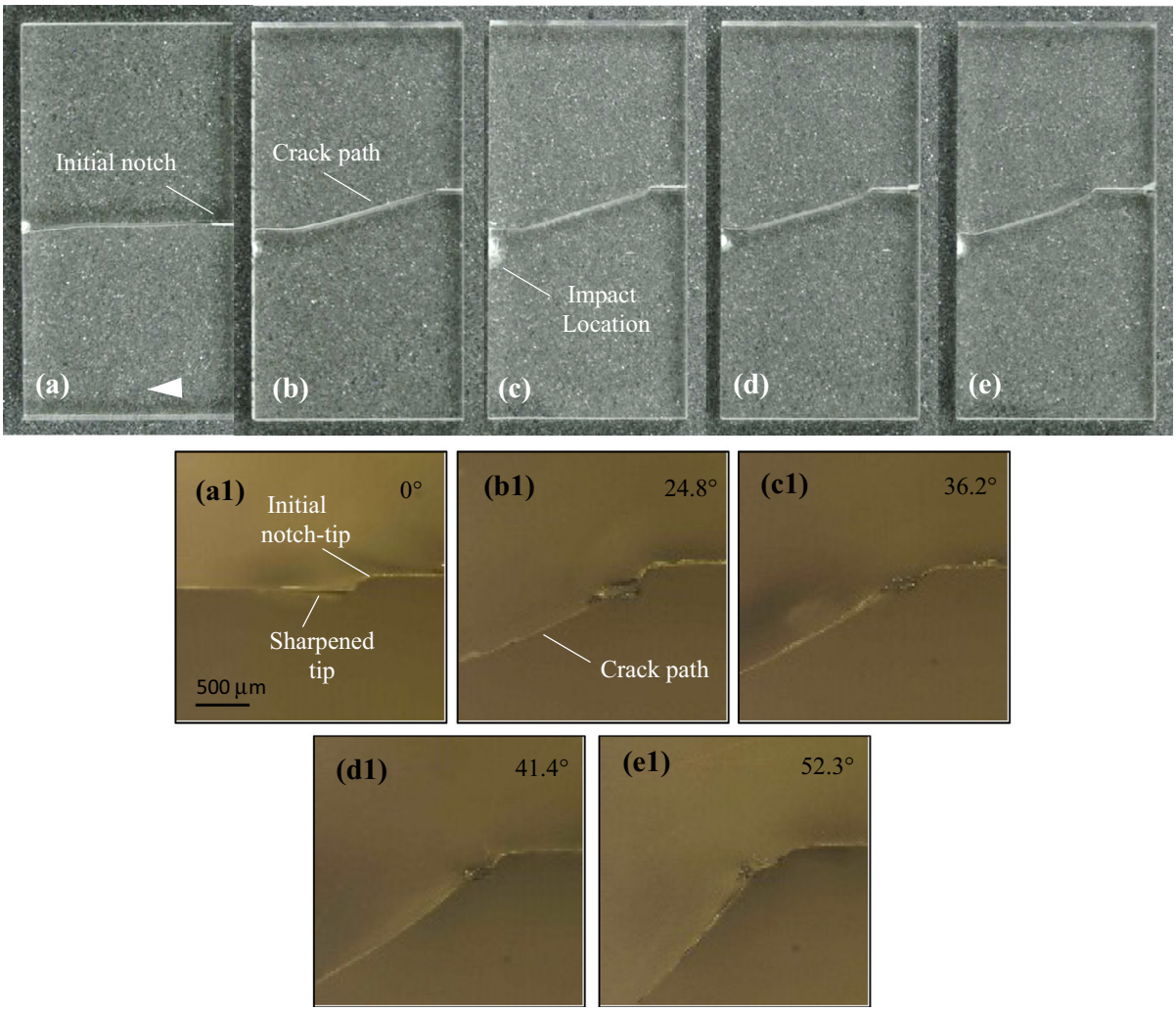

Fig. 10. (a)–(e) Photographs of fractured PMMA specimens (upper half) with config. 1–5 in sequence. (a1)–(e1) Close-up photographs of crack initiation at initial notch tip for the respective configurations showing different crack initiation angles. (Only the upper-half of the fractured specimen is shown).

Table 3
Measured crack initiation kink angle (error ± 0.3 deg) for PMMA compared with the MTS criteria.

	α_{cr} (deg.)	MTS criteria (deg.)
Config. 1	0	0
Config. 2	24.8	24.4
Config. 3	36.2	37.4
Config. 4	41.4	43.9
Config. 5	52.3	53.1

of config. 5 (see Fig. 14(b)), a monotonic increase in the magnitude of both the stress intensity factors is evident in the pre-initiation period. The mode-II stress intensity factors are negative, consistent with the loading configuration employed. Further, for about 10 μs prior to crack initiation, the mode-II stress intensity factors vary only modestly when compared to the mode-I counterparts. After crack initiation, the mode-I stress intensity factors continue to increase whereas the mode-II stress intensity factors precipitously drop to zero before changing sign as the emanating stress waves from the propagating crack-tip bounce off the free edges of the sample and interfere with the crack-tip fields. Finite element simulations for this configuration were carried out to extract the mixed-mode stress intensity factors independently until crack initiation [17]. The details of the simulation are reported in Appendix A. The computed mode-I stress intensity factor corresponding to the

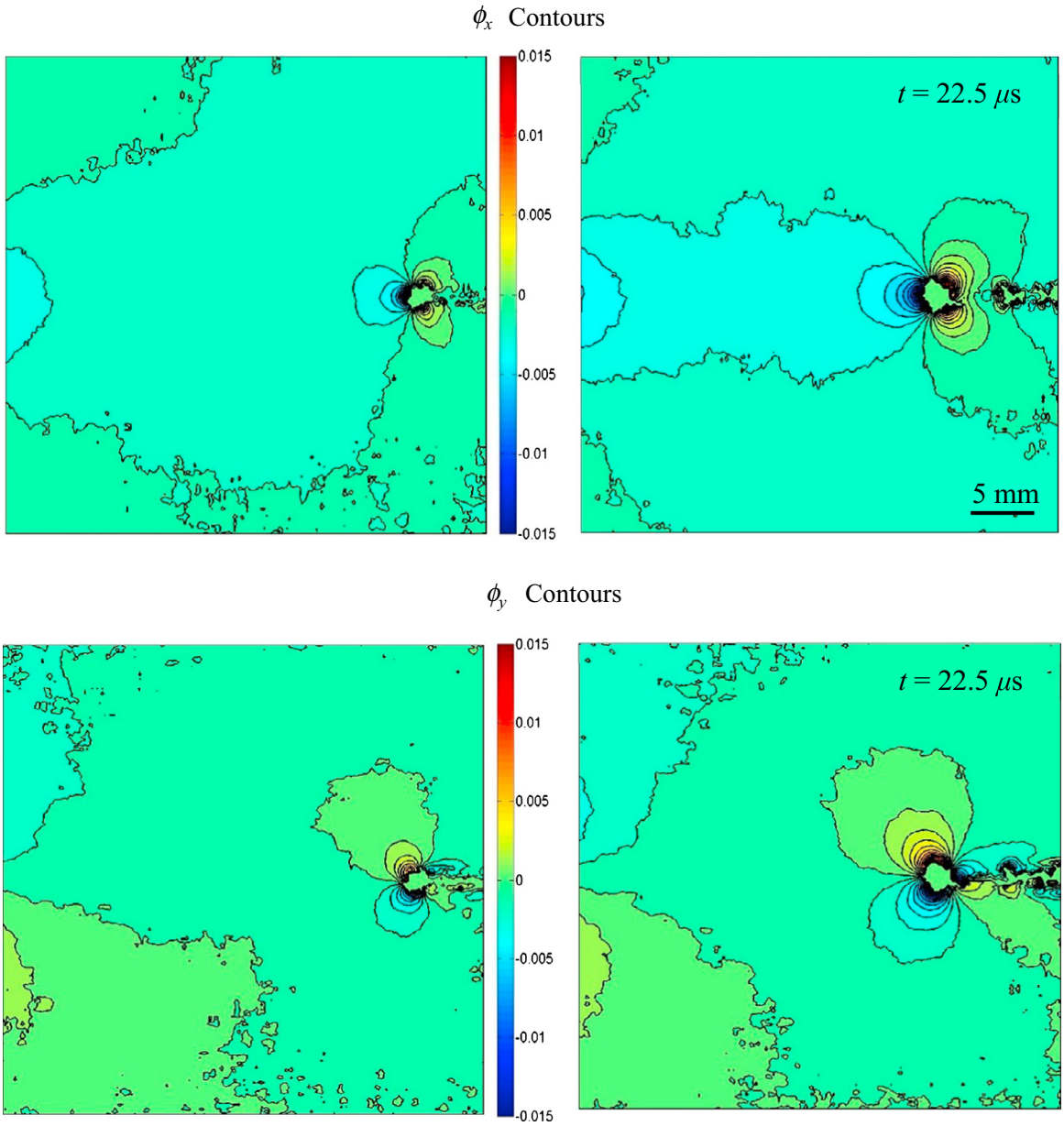

Fig. 11. Angular deflection contour plots (contour interval = 5×10^{-4} rad) proportional to stress gradients of $(\sigma_{xx} + \sigma_{yy})$ in the x- and y-directions for a PMMA specimen with $a = 6$ mm and $e = 0$ mm. (Note that $t = 0$ in these correspond to the instant at crack initiation.)

one obtained experimentally was matched at $t = 0$ as shown in Fig. 14. The remaining pre-initiation values for both mode-I and mode-II in Fig. 14 show a good match with the other experimental counterparts.

A compilation of mode-I and mode-II stress intensity factor histories evaluated from DGS for all configurations are plotted in Fig. 13(b). Again, the time axis of each experiment was shifted such that $t = 0$ corresponds to the instant at which the crack initiated at the initial notch tip as determined from the recorded images. It can be seen that there is a monotonic reduction in its magnitude of K_I at initiation from config. 1 to config. 5. The K_{II} histories, on the other hand, show an opposite trend with a monotonic increase in magnitude of K_{II} at initiation from config. 1 to config. 5. Further, in the window of observation, K_{II} values approximately reach a plateau prior to crack initiation. In the post-initiation period, K_I histories continue to increase while a precipitous drop in K_{II} occurs in all cases. An oscillatory decaying trend in K_{II} about zero is also evident suggesting crack growth preference to mode-I. These are in line with predictions based on computations described in the earlier section where an increase in the shear stress and a decrease in the normal stress at the prospective crack-tip were seen when located father away from the free edge (longer crack). Table 4 shows the time rate of change of SIFs $\dot{K}$ in the pre-initiation regime

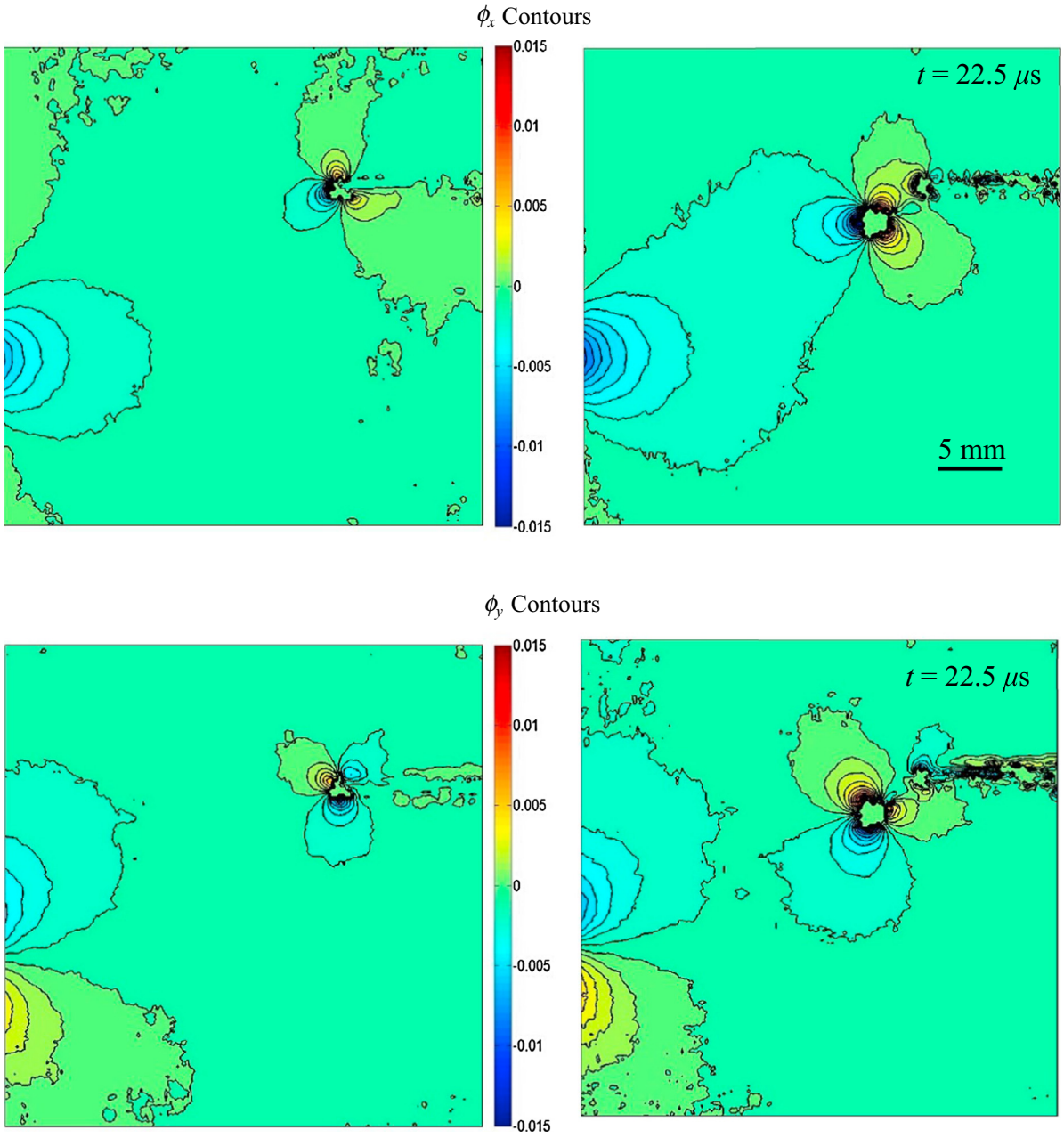

Fig. 12. Angular deflection contour plots (contour interval = 5×10^{-4} rad) proportional to stress gradients of $(\sigma_{xx} + \sigma_{yy})$ in the x- and y-directions for a PMMA specimen with a = 15 mm and e = 15 mm. (Note that $t = 0$ in these correspond to the instant at crack initiation).

based on values from -5 μs to 0 μs. Evidently $\dot{K}_{II}$ values close to initiation are relatively small in magnitude when compared to $\dot{K}_I$. The $\dot{K}_I$ values show a reduction from config. 1 to config. 5 but all in the range $\sim 10^4$ MPa$\sqrt{\text{m}}$ s^{-1}. These experiments were quite repeatable as detailed in Appendix C).

5. Mixed-mode fracture of polycarbonate

5.1. Specimen preparation, geometry, image analysis

The fracture behavior of polycarbonate (Lexan-9034 from Sabic; elastic modulus 3.64 GPa, Poisson's ratio 0.37 and density 1200 kg/m^3) was studied next. SEN specimens were prepared to carry out the dynamic fracture experiments as with

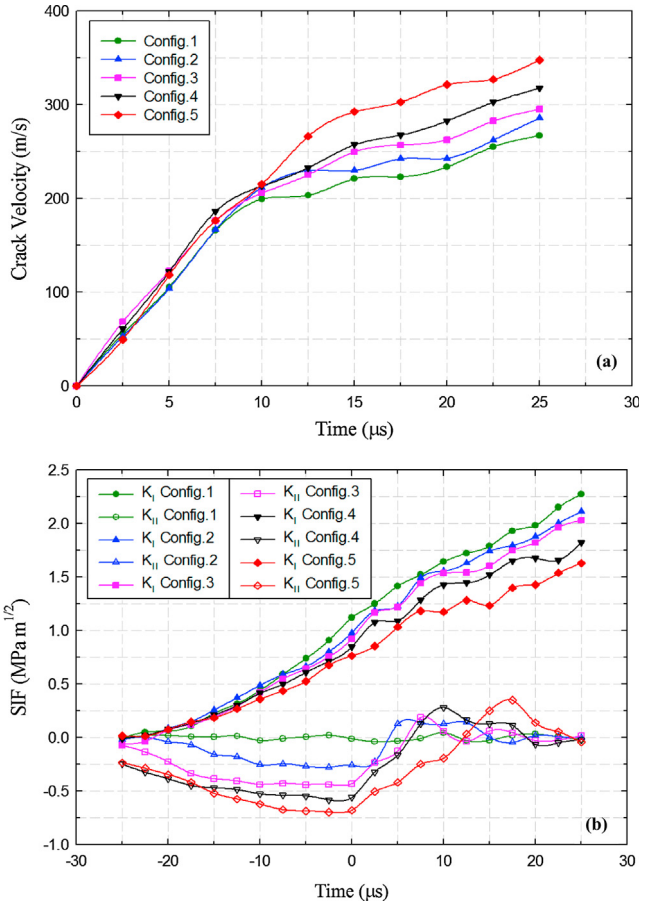

Fig. 13. Compilation of (a) crack velocity and (b) stress intensity factor (SIF) histories for all PMMA configurations. (K_{II} for config. 1 should be ideally zero and the associated deviations provide an estimate of errors for other configurations.)

PMMA. The specimens were 100 mm × 50 mm × 6.15 mm plates machined from commercially procured sheet as shown in Fig. 6. An initial notch was machined into the specimens using a diamond impregnated circular saw and further sharpened using a razor blade similar to the PMMA counterparts. The crack length and location of the initial notch tip was varied as in PMMA counterparts to generate various mode-mixities (see Fig. 6 for details). Five different configurations (same as the ones used for PMMA) were used to produce various mode-mixities at initiation. Image analysis and experimental setup were the same as PMMA counterparts described earlier except for the striker velocity used during experiments. A higher striker velocity of ~17.5 m/s was used in all the experiments for polycarbonate in order to be able to initiate the crack in this relatively tough polymer. To evaluate the fracture parameters of polycarbonate using transmission DGS, its elasto-optical constant C_σ had to be evaluated first. The details of the same are reported in Appendix B and C_σ was found to be $-1.33 \pm 0.04 \times 10^{-10}$ m^2/N for polycarbonate.

5.2. Results

5.2.1. Crack path and deformation histories

Photographs of five fractured samples from each of the configurations are shown in Fig. 15(a)–(e). The stress wave loading occurred at the left edge of the specimen. The crack initiated from the initial crack-tip and propagated from the right edge of the specimen towards the left as shown by the arrowhead. In each case the crack initiated and kinked at a different angle. In Fig. 15(a), due to symmetric loading configuration, the crack propagated in a mode-I condition throughout until it approached the free edge and deviated from its path. In Fig. 15(b)–(e) the crack has initiated and propagated in mixed-mode. Fig. 15(a1)–(e1) shows the close-up of the initial crack-tip vicinity. As in PMMA, it can be seen that the crack initiation angle monotonically increased from config. 1 to config. 5 (0°, 17.4°, 25.1°, 29.4°, 39.8°). This clearly shows that the crack initiation angle and hence mode-mixity changes with increase in crack length. The kink angles however were not as large as in PMMA (0°, 24.8°, 36.2°, 41.4°, 52.3°) counterparts although experiments were repeatable. Higher fracture toughness of polycarbonate relative to PMMA and the differences in crack initiation mechanics due to its ductility are potentially responsible

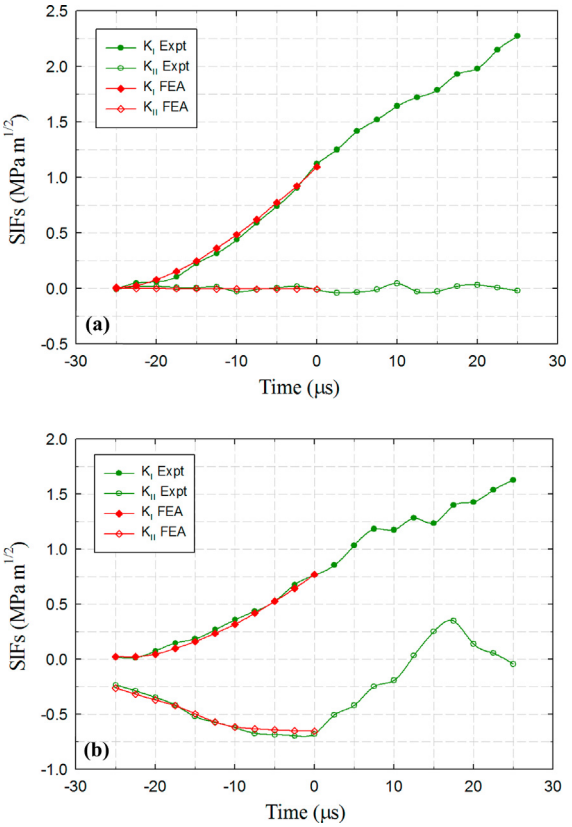

Fig. 14. Stress intensity factors (SIFs) evaluated from experiments and finite element analysis for (a) config. 1 (a = 6 mm, e = 0 mm) and (b) config. 5 (a = 15 mm, e = 15 mm). (t = 0 corresponds to crack initiation.)

Table 4
Time rate of change of SIFs for different mixed-mode PMMA configurations.

	$\dot{K}_I$ (GPa$\sqrt{}$m/s)	$\dot{K}_{II}$ (GPa$\sqrt{}$m/s)
Config. 1	85.2	−0.2
Config. 2	70.8	−1.4
Config. 3	64.4	−0.3
Config. 4	54.1	−1.9
Config. 5	34.9	−0.6

for these differences. The crack initiation angle predicted by the MTS criterion was also evaluated and is listed in Table 5. There is a good agreement between the observed crack initiation angle and the MTS criterion for only config. 2 but deviate significantly in others.

Contour plots of measured angular deflection contours ϕ_x and ϕ_y proportional to orthogonal stress gradients $(\sigma_{xx}+\sigma_{yy})_{,x}$ and $(\sigma_{xx}+\sigma_{yy})_{,y}$ obtained from DGS for two select configurations namely, config. 1 and config. 2 are shown in Figs. 16 and 17, respectively. For brevity, plots for two select time instants, one at crack initiation and the second during propagation, are presented. (The contour levels and the scale bar are shown in the first plot in each set and are applicable to the other plots as well.) In these t = 0 μs represents the time at which the crack initiated at the original sharpened tip. In each figure, top and bottom rows correspond to ϕ_x and ϕ_y, respectively. Fig. 16 shows the angular deflection contours for config. 1 (a = 6 mm; e = 0 mm). The crack followed nearly a straight path during the window of observation. It can be seen that the overall size of the contour increased during propagation suggesting an increase in stress intensity factors. The partial contours seen on the left edge of the plot are due to the line-load from the long-bar. Fig. 17 shows the angular deflection contours for config. 5 (a = 15 mm; e = 15 mm). The crack initiated at an angle suggesting mode-mixity at initiation. At time t = 0 μs the angular deflection contours turned towards the direction of crack initiation. The overall size of the contours increased during the observation window implying an increase in the magnitude of the effective stress intensity factors.

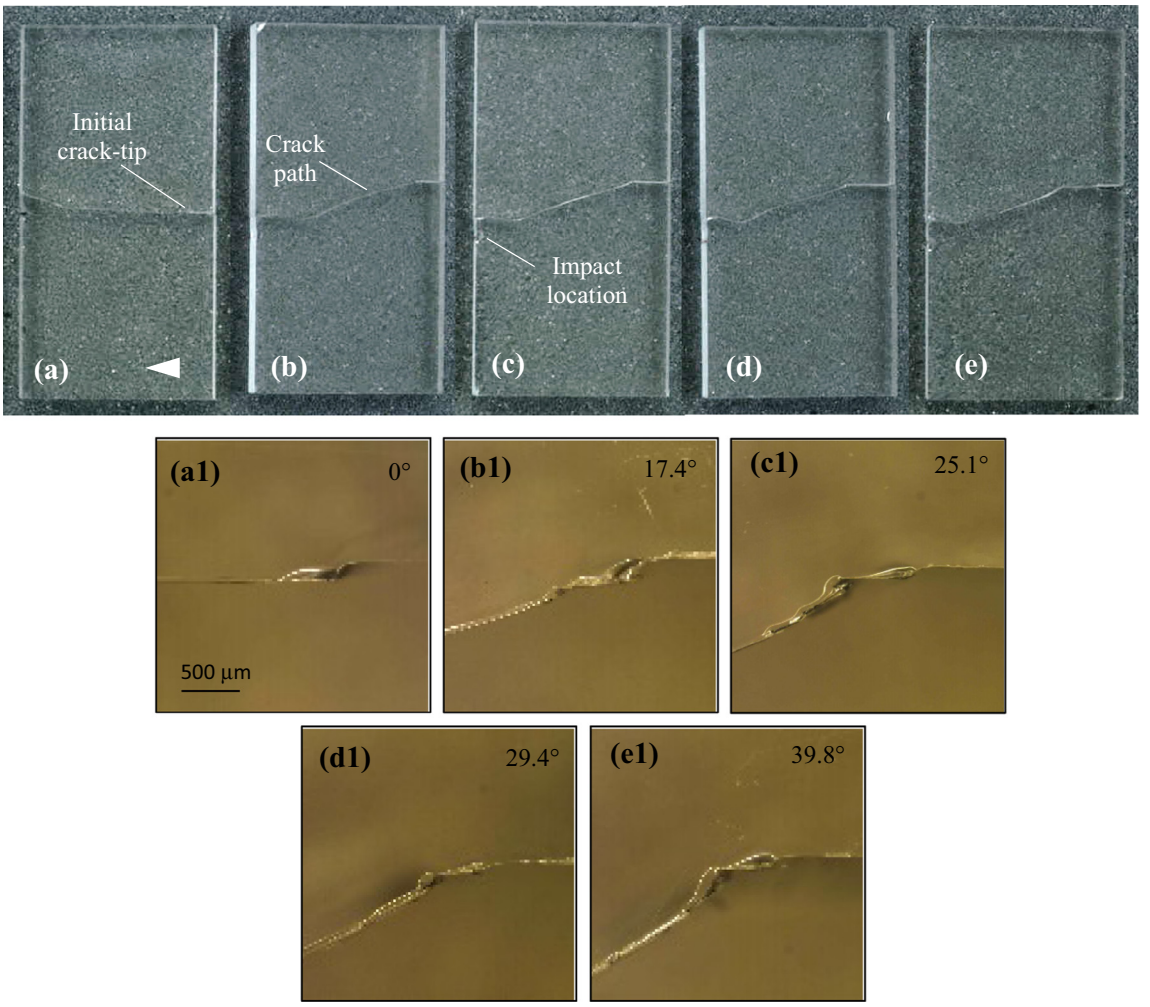

Fig. 15. (a)–(e) Photographs of fractured polycarbonate specimens (upper half) with config. 1–5 in sequence. (a1)–(e1) Close-up view of crack initiation at the initial notch tip for the respective configurations with the measured crack initiation angle.

Table 5
Measured crack initiation angles (error ± 0.3 deg.) for polycarbonate specimen compared with MTS criteria. (Larger discrepancy between the two in mixed-mode case is attributed to ductility of polycarbonate.)

	α_{cr} (deg.)	MTS criteria (deg.)
Config. 1	0	0
Config. 2	17.4	17.8
Config. 3	25.1	34.2
Config. 4	29.4	40.1
Config. 5	39.8	46.7

5.2.2. Crack velocity and stress intensity factor histories

A compilation of crack velocity histories for all the configurations are shown in Fig. 18(a). The overall trends are similar to those for PMMA shown in Fig. 13(a). At the end of the window of observation, which is $t = 25$ μs, the final crack velocity monotonically increased from 340 m/s in config. 1 to 458 m/s in config. 5. This again is similar to the observation made for PMMA that the crack tends to travel faster with increasing mode-mixity. When compared to PMMA counterparts for each configuration, the crack travels faster in PC, attributed to the higher impact velocity used during PC tests compared to PMMA.

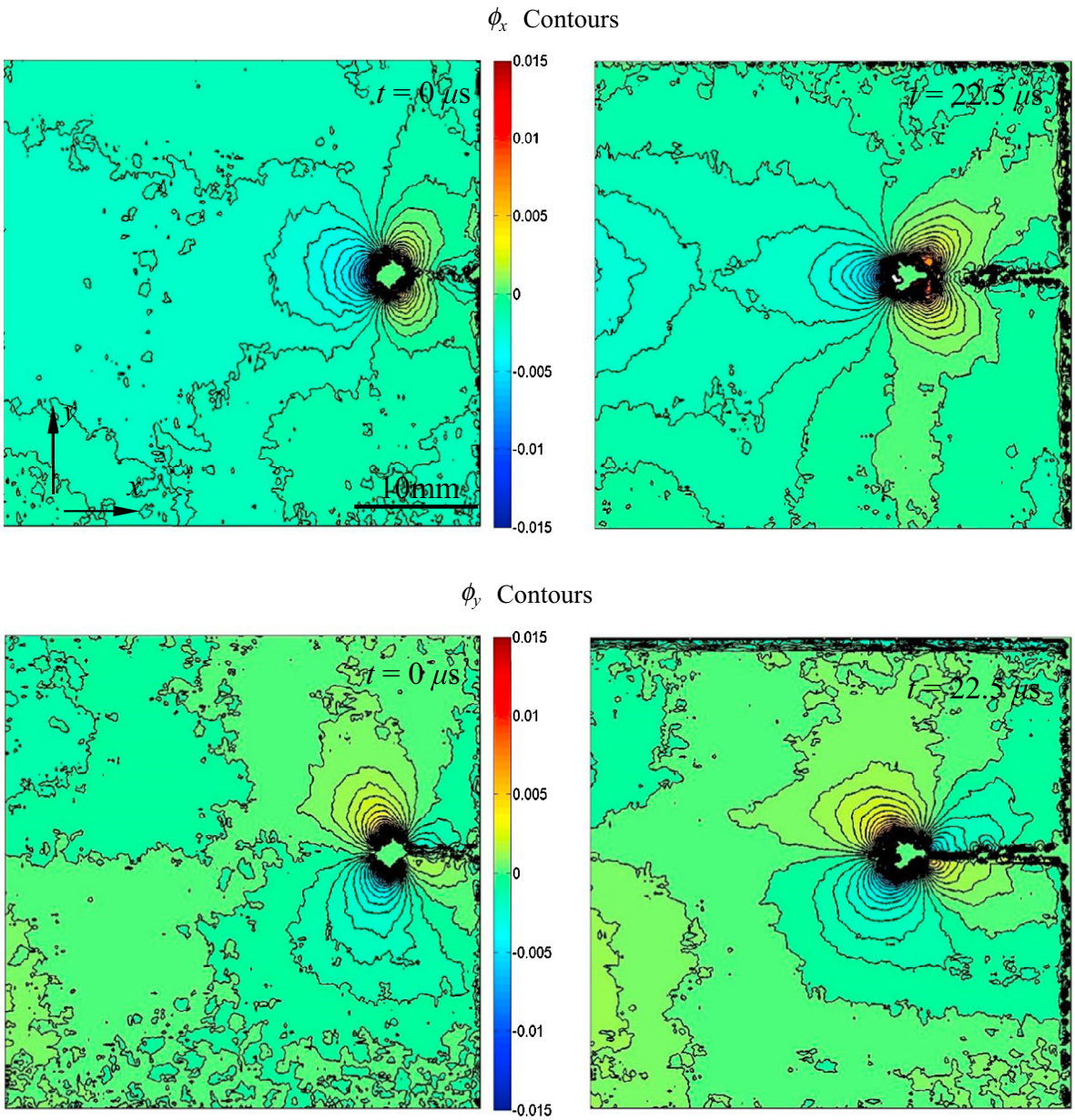

Fig. 16. Angular deflection contour plots (contour interval = 5×10^{-4} rad) proportional to stress gradients of $(\sigma_{xx} + \sigma_{yy})$ in the x- and y-directions for a polycarbonate specimen with $a = 6$ mm and $e = 0$ mm.

Both mode-I and mode-II stress intensity factor histories (K_I and K_{II}) evaluated form DGS for all configurations are plotted in Fig. 18(b). Time $t = 0$ corresponds to the instant at which the crack initiated. As in the PMMA counterparts (Fig. 13(b)) K_I values increased monotonically after impact until crack initiation and the values were lower for a longer initial notches at a given instant. The critical K_I values at crack initiation were consistently higher in each of the cases when compared to the PMMA counterpart. Further, the critical K_I values decreased with the initial crack length (config. 1 to config. 5). The post crack initiation ($t > 0$) K_I values continued to increase but at different and lower rates in each geometry. The K_{II} histories on the other hand showed an opposite trend. Prior to crack initiation, the K_{II} values are nearly constant for each configuration, the highest magnitude corresponding to the case with the deepest initial edge crack. That is, a continuous increase in K_{II} values at initiation from config. 1 to config. 5 are evident. This trend is in line with the numerical predictions for different geometries where an increase in shear stress and a decrease in normal stress were seen at the prospective crack-tip locations of longer cracks (as described earlier). After the crack initiated ($t = 0$), a sustained drop in the magnitude of K_{II} values towards zero occurred in all cases suggesting the tendency for crack growth to occur in mode-I. As in PMMA counterparts, K_{II} histories

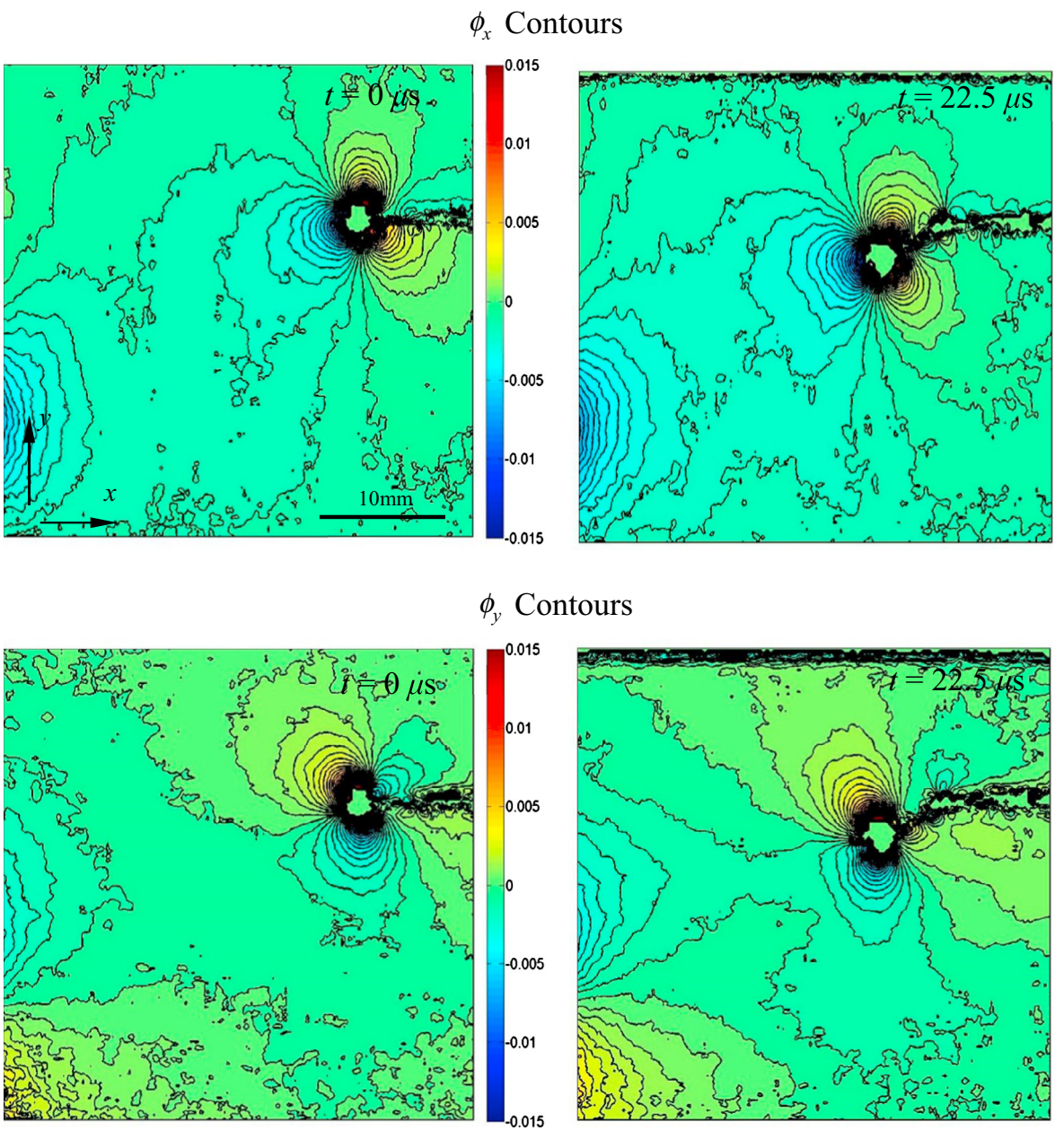

Fig. 17. Angular deflection contour plots (contour interval = 5×10^{-4} rad) proportional to stress gradients of $(\sigma_{xx} + \sigma_{yy})$ in the x- and y-directions for a polycarbonate specimen with a = 15 mm and e = 15 mm.

for polycarbonate show an oscillatory behavior about zero in the post-initiation period. Polycarbonate being a tough polymer relative to PMMA the magnitudes of both K_I and K_{II} are significantly higher. The time rate of change of SIFs ($\dot{K}$) in the pre-initiation regime are presented in Table 6. As in the PMMA counterparts, the values of $\dot{K}$ and $\dot{K}_{II}$ were obtained from data $t = -5$ to 0 μs. Again, the magnitudes of $\dot{K}_{II}$ values close to initiation are smaller than $\dot{K}_I$ in all mixed-mode configurations but higher than the PMMA counterparts due to higher impact velocity used.

5.3. Discussion

The enlarged crack-tip images shown in Fig. 19(a) for different specimen configurations provide details about crack initiation and growth in PMMA. For clarity, one half (the upper half) of the fractured sample is shown. At this magnification, the dynamically grown crack edges appears relatively sharp in each of these images without any strong indication of crazing as

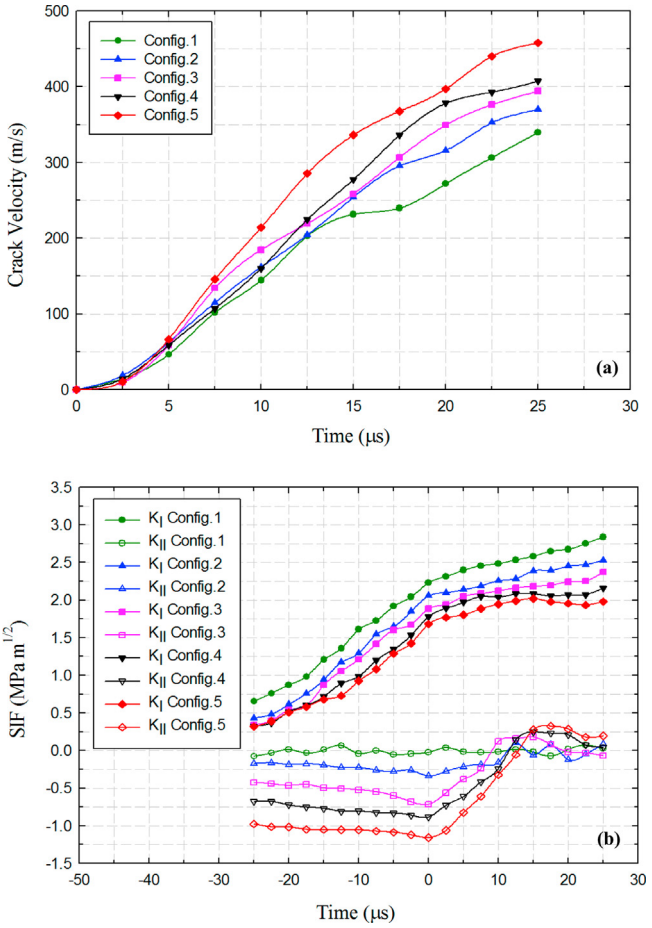

Fig. 18. Compilation of (a) crack velocity and (b) stress intensity factor (SIF) histories for all the configuration for dynamic fracture of polycarbonate.

Table 6
Time rate of change of SIFs for different polycarbonate mixed-mode configurations.

	$\dot{K}_I$ (GPa$\sqrt{}$m/s)	$\dot{K}_{II}$ (GPa$\sqrt{}$m/s)
Config. 1	65.2	−3.2
Config. 2	68.3	−10.3
Config. 3	64.6	−14.4
Config. 4	76.8	−9.4
Config. 5	82.1	−12.6

whitened regions adjacent to the crack flanks, consistent with a brittle fracture behavior. Further, the crack initiation angles match the ones computed using the MTS criteria. On the other hand, Fig. 16 shows polycarbonate counterparts in the crack-tip vicinity. When compared to PMMA, the crack flanks after initiation show visible whitening and rugged morphology indicating crazing and ductility (see Fig. 19(a)). This characteristic is similar to the ones reported in [3]. Further, during initial crack growth, staircase/stepped patterns along the crack path are evident (see Fig. 19(b)) suggesting an intermittent growth/arrest mechanism at crack initiation. Considering all these toughening mechanisms, the match between the measured kink angle and the prediction based on brittle fracture criteria is rather poor.

The critical values of stress intensity factors K_I and K_{II} were plotted as a fracture envelope of the functional form $f(K_I, K_{II}) = 0$ in Fig. 20. Such an envelope could be considered as an extension of the ones for quasi-static conditions with inertial effects entering the results through measured stress intensity factors [22]. *At least two data points for each loading configuration are included for both PMMA and polycarbonate*. The data sets were fitted with an equation of the form $\left(\frac{K_I}{K_{I-cr}}\right)^2 + \left(\frac{K_{II}}{K_{II-cr}}\right)^2 = 1$ and the corresponding fits are shown in the Fig. 20. The $K_{I\text{-cr}}$ for mode-I crack initiation in case of polycarbonate reported here (2.25 MPa$\sqrt{}$m) is in agreement with the sharpest crack case reported in [23].

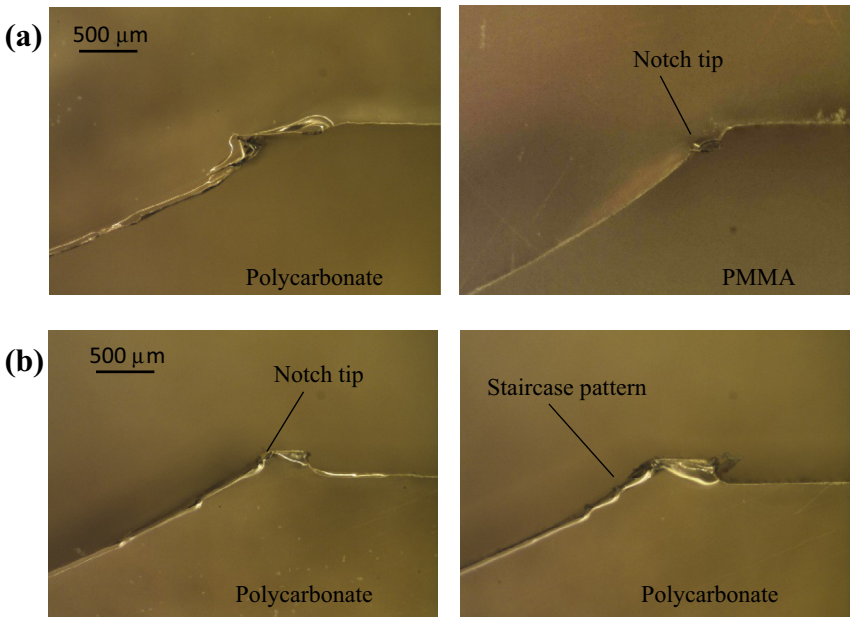

Fig. 19. Distinct characteristics observed in polycarbonate. (a) Ductile and brittle failures observed in polycarbonate and PMMA respectively. (b) Staircase/stepped pattern at initiation observed in polycarbonate.

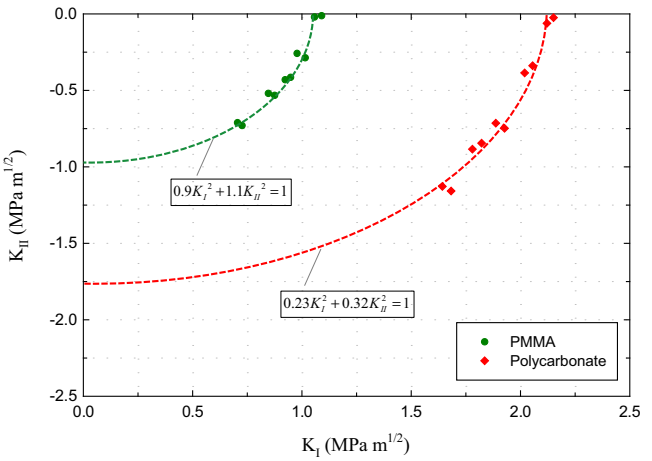

Fig. 20. Curve fitted fracture envelopes for PMMA and polycarbonate based on measured stress intensity factors at crack initiation.

For nominally brittle materials, the dynamic crack growth toughness is a function of crack speed, loading rate ($\dot{K}$) and temperature [24]. Most reported experimental results thus far are only for mode-I conditions and for different brittle (polymers) and a few ductile (steels) materials and not for mixed-mode conditions. Accordingly, using measured post-initiation stress intensity factors K_I and K_{II} and instantaneous crack speeds V in Figs. 13 and 18, the dynamic mixed-mode energy release rates for growing cracks were evaluated as [24],

$$G = \frac{1}{E}\left[A_I(V)K_I^2 + A_{II}(V)K_{II}^2\right] \tag{7}$$

where $A_I = \frac{V^2\alpha_L}{(1-\nu)C_S^2 D}$, $A_{II} = \frac{V^2\alpha_S}{(1-\nu)C_S^2 D}$, $D = 4\alpha_L\alpha_S - (1+\alpha_S^2)^2$ and other parameters have been defined previously. Plots of G vs. V for both PMMA and polycarbonate are shown in Fig. 21(a) and (b). Although the uniqueness of such a plot has not been fully established, some basic features can be inferred from the data. The G values, including those for mode-I, show an increasing trend with crack velocity similar to other brittle polymers (e.g., Homalite-100, epoxy). The rate of increase, however, decreases in higher mode-mixity cases (configs. 2–5) causing mixed-mode G data to fan out. Thus, based on these limited

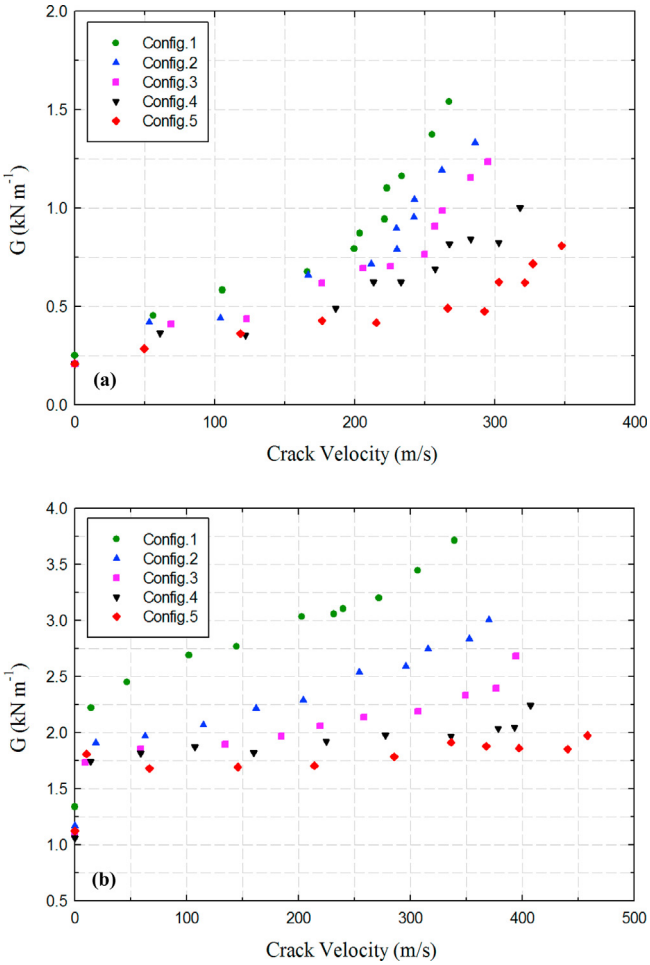

Fig. 21. Plot of mixed-mode dynamic strain energy release rates (G) with crack velocity (V) for all configurations of (a) PMMA, and (b) polycarbonate

data sets, the possibility of a unique mixed-mode G vs. V seems unlikely but needs to be further explored. The data for polycarbonate counterparts are shown in Fig. 21(b). The overall trends are similar to those for PMMA with the exception of a distinct jump in the G values immediately after crack initiation in each case. This is attributed to the crack tip ductility of polycarbonate alluded to in the micrographs shown in Fig. 19 and is similar to the behavior observed in some carbon steels [24].

6. Conclusions

In this work, mixed-mode dynamic fracture behaviors of two widely used polymers, PMMA and polycarbonate, have been investigated using a relatively new full-field optical method, Digital Gradient Sensing (DGS), and ultrahigh-speed digital photography to visualize and quantify crack initiation and growth behaviors. Finite element analyses have also been carried out to complement and/or supplement experiments. The following are some of the major conclusions of this work:

- Different mode-mixities at crack initiation can be generated using a simple eccentric reverse impact loading configuration involving edge cracked plates containing cracks of different lengths. At a constant impact velocity and fixed loading eccentricity, it requires only crack length increase to increase the mode-mixity at crack initiation.
- The measured histories of crack-tip parameters in various cracked geometries before and after crack initiation show that when the crack length increased for a fixed load-point eccentricity relative to the crack location, the mode-I and mode-II stress intensity factors increased monotonically up to crack initiation at an *effective* $\dot{K}$ of the order of 10^4 MPa$\sqrt{\text{m}}$ s^{-1} in both PMMA and polycarbonate.

- The crack velocity histories for PMMA and PC in the post-initiation regime show a rapid acceleration following crack initiation (over 5–10 μs). The crack speed at the end of the observation window attained by mixed-mode cracks is successively higher with mode-mixity at initiation.
- For PMMA, the mode-I stress intensity factors continued to increase following crack initiation at about the same rate as the ones prior to initiation whereas for polycarbonate the increases were at much lower rates. The mode-II stress intensity factors in PMMA increased monotonically but at a significantly lower rate relative to the mode-I counterparts prior to crack initiation with the longer cracks showing higher magnitude. Once the crack initiated, the mode-II stress intensity factors precipitously dropped (over 5–10 μs) to zero before settling to a near zero value.
- The mixed-mode stress intensity factors at initiation were compiled for each polymer type and fracture envelopes were obtained empirically based on the range of mixities achieved. Equations $0.9K_I^2 + 1.1K_{II}^2 = 1$ and $0.23K_I^2 + 0.32K_{II}^2 = 1$ describes crack initiation envelopes for PMMA and polycarbonate, respectively.
- The mixed-mode fracture behavior of PMMA in terms of crack kink direction at initiation agrees with the predictions based on the MTS criterion for brittle materials. However, the polycarbonate does not match the MTS predictions at these loading rates.
- The variation of dynamic energy release rates (G) with instantaneous crack speed (V) for different PMMA and polycarbonate specimen configurations resulted in a fan of data points instead of a single overlapping data set, suggesting G-V plots to depend on mode-mixity at crack initiation.
- The PMMA fractured samples do not show evidence of crazing or whitening and the two crack flanks remained relatively sharp and featureless after crack initiation. The polycarbonate, on the other hand, showed ductile fracture features such as visible whitening along the edges of the crack path. Further, the crack path displayed a staircase/stepped morphology suggesting an intermittent yet dynamic crack initiation.

Acknowledgments

The support of this research by the U.S. Army Research Office through grant W911NF-16-1-0093 is gratefully acknowledged.

Appendix A

A.1. Complementary finite element simulations

Complementary dynamic finite element simulations of the mode-I and mixed-mode impact tests on SEN specimen was carried out using ABAQUS®/Explicit software. The specimen geometry and loading configuration is shown in Fig. 6. Two loading configurations namely config. 1 and config. 5 were modeled. The long-bar in loading setup was also modeled for this simulation. The impact end of the long-bar was cylindrical in shape (line-load). The specimen and the long-bar were discretized into 259,337 and 37,952 solid 3D tetrahedral elements respectively. The discretized model with the crack opening displacements is shown in Fig. 22. Local seeding was adopted around the initial crack-tip to generate finer mesh around it. The time steps during the analysis were allowed to be automatically controlled by the integration scheme. Plane stress with corresponding specimen thickness was imposed on PMMA model during section assignment. The young's modulus and poison's ratio of PMMA used in this analysis was obtained from ultrasonic pulse echo measurement of longitudinal and shear wave speeds [25] and its mass density. Tables 1 and 2 shows the material properties of PMMA and the AL-7075 aluminum long-bar used in the simulation, respectively. The particle velocity obtained from strain gauge readings on the Hopkinson pressure bar experiment was input into the analysis. The recorded strain history is shown in Fig. 22(b). The crack opening (v) and crack sliding (u) displacements were extracted along the two crack faces. This was repeated for each displacement step. The apparent mode-I and mode-II stress intensity factors, $(K_I)_{app}$ and $(K_{II})_{app}$ at each step were computed using [16],

$$(K_{I,II})_{app} = \frac{E\sqrt{2\pi}}{8\sqrt{r}}(v\,;u);(r,\theta=\pi) \tag{A1}$$

Appendix B

B.1. Evaluation of elasto-optic constant for polycarbonate

B.1.1. Experimental details

Elasto-optic constant of Lexan-9034 was evaluated using a line-load acting on an edge of a large planar sheet (approximating a classical Flamant problem). A rectangular sheet of 100 mm × 75 mm of thickness 6.15 mm was placed on a flat rigid platform and subjected to a line-load as shown in Fig. 23. An Instron 4465 universal testing machine was used for loading the specimen in displacement control mode (crosshead speed of 0.005 mm/s). A target plate coated with random black and white speckles was placed behind the specimen at a distance of 28.1 mm from the mid plane of the specimen. A Nikon

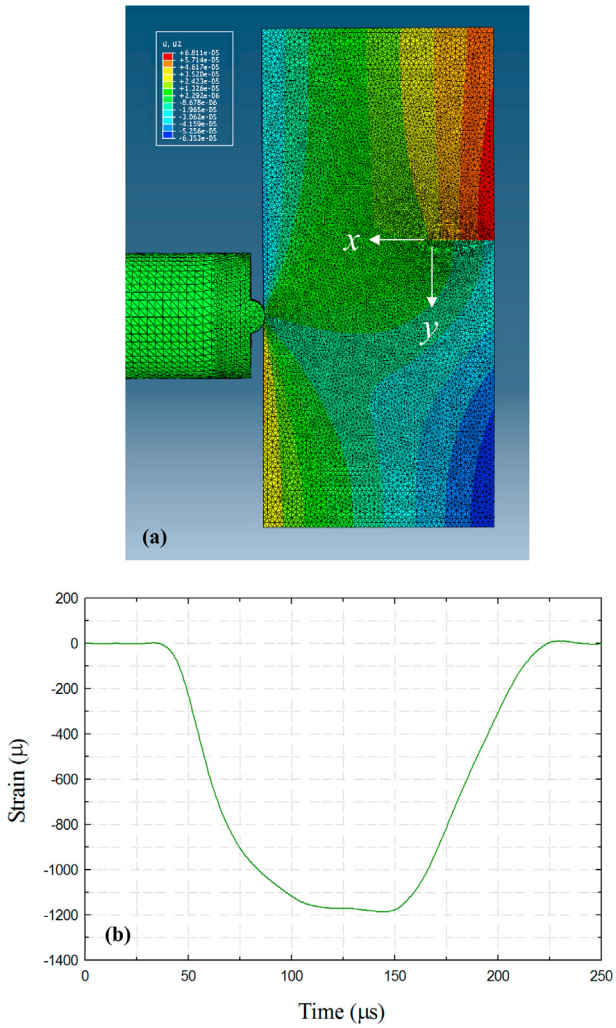

Fig. 22. (a) Discretized finite element model of config. 5 (a = 15 mm; e = 15 mm) for PMMA with an overlay of displacement contours in the y-directions. (b) The strain history recorded on the Hopkinson bar used as input into the FE simulation.

D100 digital SLR camera fitted with a 70–300 mm focal length lens and extension tube was used to record the speckles. The camera was placed in front of the specimen at a distance (L) of ~900 mm with the camera focused on a uniformly illuminated target plane through the specimen. A camera resolution of 1504 × 1000 pixels was used to acquire 8 bit images.

An undeformed image of the target plate through the specimen was recorded at no-load condition (1 pixel ~ 30 μm on the target plane). As the sample was loaded, the deformed images of the target plate were recorded at 300 N, 600 N, 900 N and 1200 N loads. Two representative speckle patterns, one in the no-load state and the other in the deformed state, are shown in Fig. 24. Sufficient care was exercised to obtain a near Gaussian distribution of gray scales for each image in the mid-range of 0–255 (8 bit) scale by adjusting the illumination and the numerical aperture of the lens. The speckles are noticeably distorted in Fig. 24(b) at top of the specimen near the concentrated load.

The digitized speckle images (1504 × 1000 pixels) in the deformed state was correlated with the image from the undeformed state using ARAMIS®. A sub-image size of 25 × 25 pixels with an overlap of 20 pixels (i.e., step size of 5 pixels) was used during image correlation. The angular deflection contours in the horizontal (x-z) and vertical (y-z) planes (global coordinate system) for a compressive load of 1200 N is shown in Fig. 25.

The angular deflections measured in two in-plane orthogonal direction are related to stresses as [11],

$$\phi_x = C_\sigma \frac{2F}{\pi} \frac{\cos(2\theta)}{r^2}$$
$$\phi_y = C_\sigma \frac{2F}{\pi} \frac{\sin(2\theta)}{r^2} \tag{B1}$$

where C_σ is the elasto-optic constant, F is the applied load, B is the specimen thickness and (r, θ) denote the polar coordinates relative to the loading point. The C_σ evaluated along ±45° for ϕ_y and 0° for ϕ_x for an applied load of 300 N is plotted

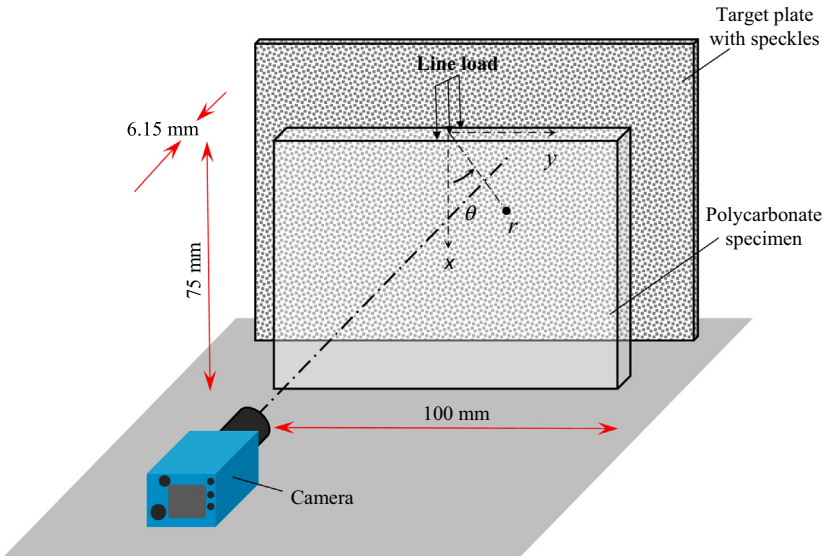

Fig. 23. Experimental setup for line loading on a polycarbonate sheet to evaluate elasto-optic constant.

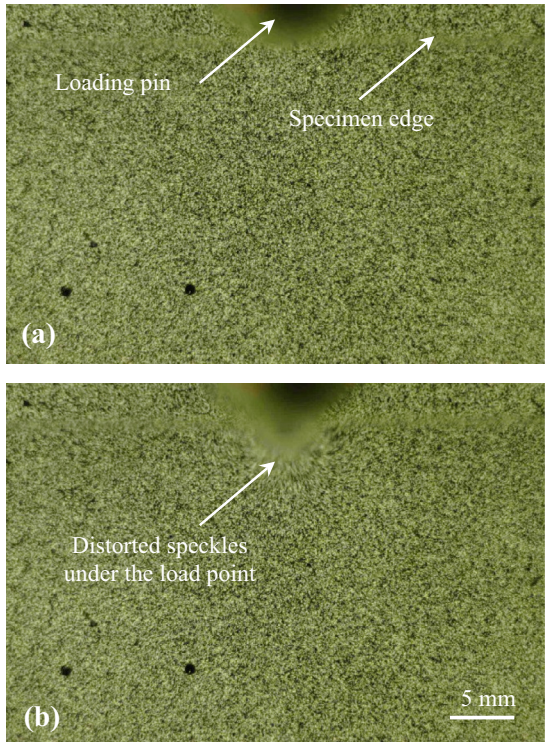

Fig. 24. Speckle images of a polycarbonate sheet under the line-load: (a) Undeformed and (b) deformed.

against r/B ratio in Fig. 26. The far field values of the angular deflections were forced to be zero based on the known boundary conditions. This accounted for any potential rigid body motions that occurred while conducting the experiments. It can be seen that there is a drop in the magnitude of C_σ from $0 < r/B < 0.5$. In the $0.5 < r/B < 2.0$ range it is nearly a constant, beyond which it again deviates due to far-field effects unaccounted for in Eq. (B1). Similar analyses for other loads were also carried out and the averaged value of C_σ was $-1.33 \pm 0.04 \times 10^{-10}$ m^2/N.

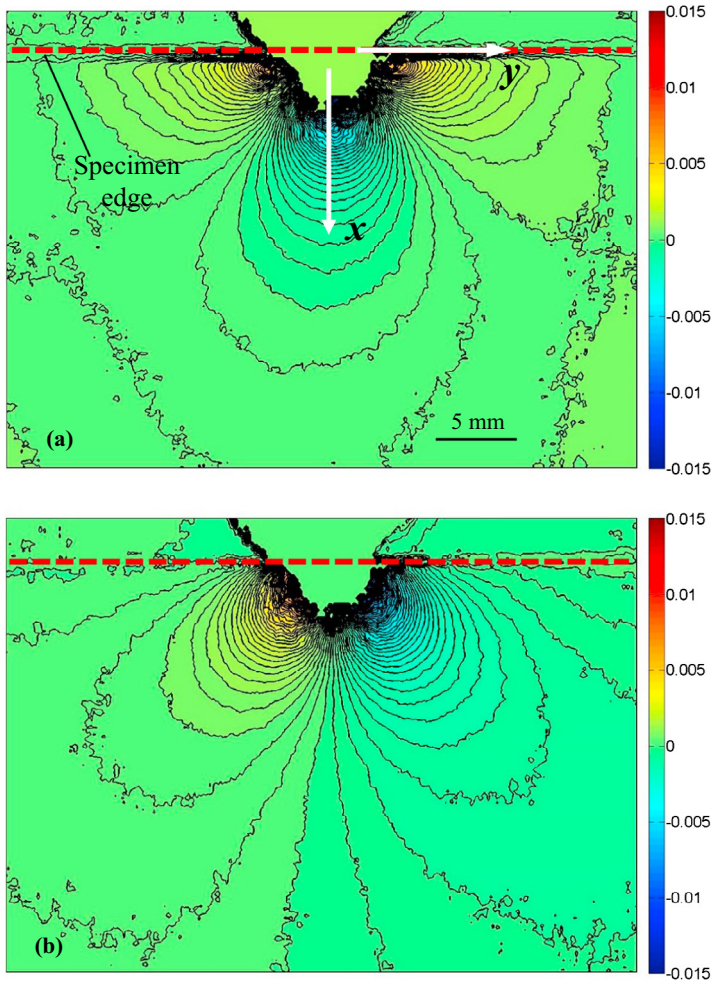

Fig. 25. Angular deflection contour plots (contour interval = 2×10^{-4} rad) proportional to stress gradients of $(\sigma_{xx} + \sigma_{yy})$ in the (a) x- and, (b) y-directions for a polycarbonate specimen under the line-load (=1200 N).

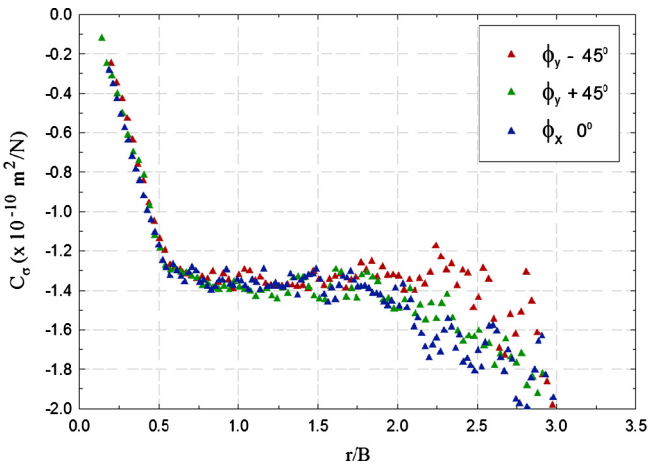

Fig. 26. Variation of elasto-optical constant C_σ evaluated at 300 N load for polycarbonate.

Appendix C

Multiple experiments were conducted to ensure repeatability in terms of dynamic fracture behavior as well as fracture parameters. Fig. 27(a)–(e) shows photographs of two fractured samples of PMMA of each configuration. A high degree of reproducibility in crack paths throughout the fracture event is clearly evident. SIF histories for two different samples of config. 1 and config. 5 are shown in Fig. 28. Again, repeatability can be readily seen in the measured values of SIFs. The slope

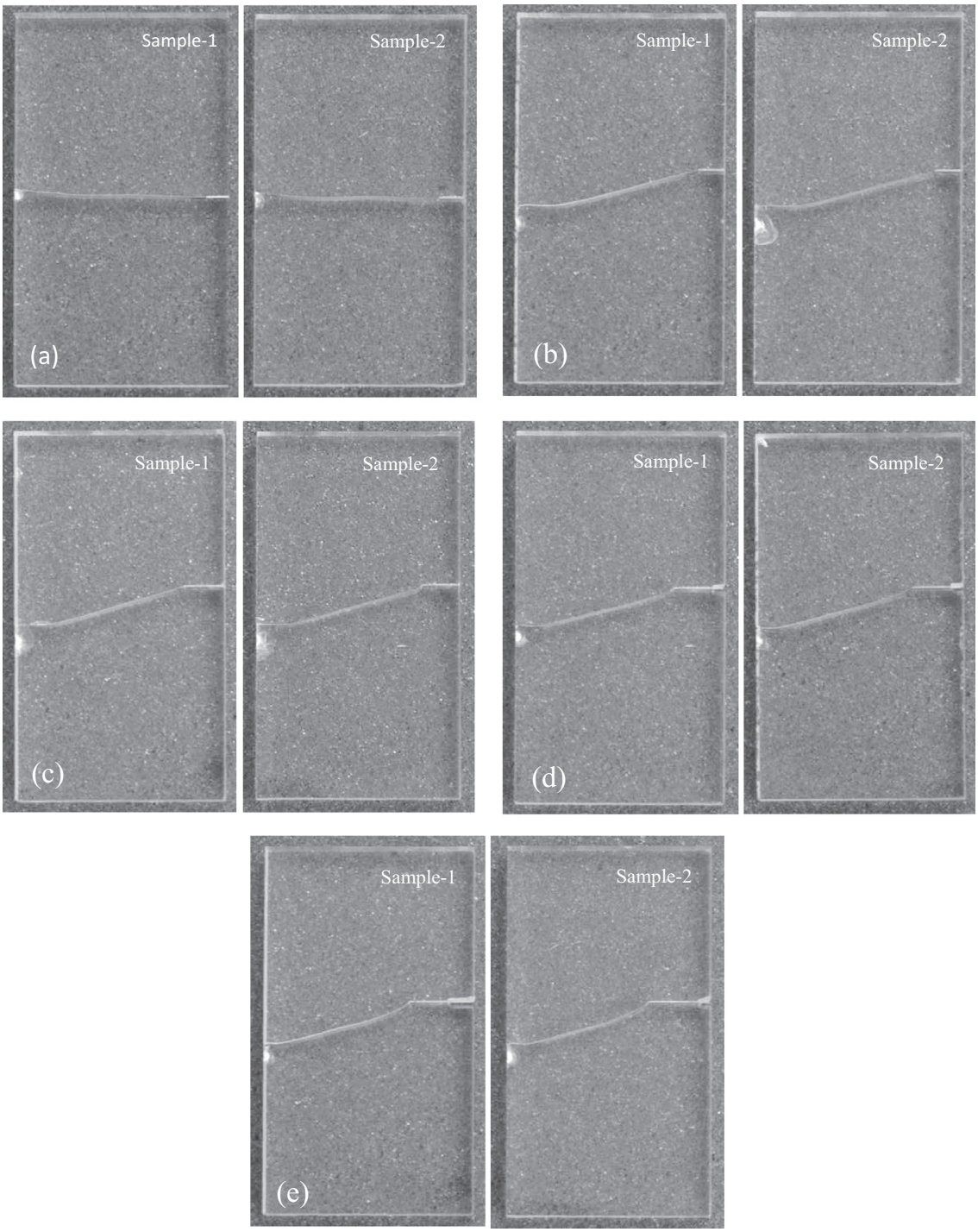

Fig. 27. (a)–(e) Multiple fractured samples of config. 1 to config. 5 respectively.

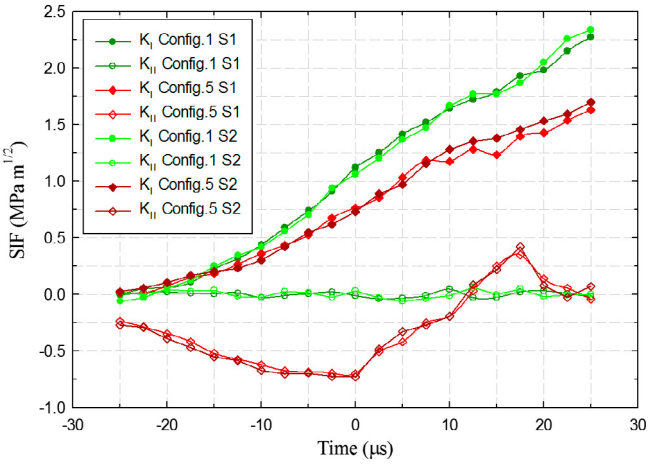

Fig. 28. SIF histories for multiple fractured samples of each configuration. The vertical broken lines denote the crack tip vicinity.

in the pre-initiation regime, the values of SIFs at crack initiation, and the slope in post-initiation regime are in good agreement.

References

[1] Kalthoff JF. Shadow optical analysis of dynamic shear fracture. Opt Eng 1988;27(10):835–40.
[2] Ravi-Chandar K. On the failure mode transition in polycarbonate under dynamic mixed-mode loading. Int J Solids Struct 1995;32(6–7):925–38.
[3] Rittel D, Levin R. Mode-mixity and dynamic failure mode transitions in polycarbonate. Mech Mater 1998;30(3):197–216.
[4] Kalthoff JF. Modes of dynamic shear failure in solids. Int J Fract 2000;101(1):1–31.
[5] Wang XK, Wei SC, Xu BS, Chen Y, Yan X, Xia HH. Transparent organic materials of aircraft cockpit canopies: research status and development trends. Mater Res Innovations 2015;19. p. S10-199–S10-206.
[6] Foster M, Love B, Kaste R, Moy P. The rate dependent tensile response of polycarbonate and poly-methylmethacrylate. J Dyn Behav Mater 2015;1 (2):162–75.
[7] Rossmanith HP. How 'mixed' is dynamic mixed-mode crack propagation? – a dynamic photoelastic study. J Mech Phys Solids 1983;31(3):251–60.
[8] Mason JJ, Lambros J, Rosakis AJ. The use of a coherent gradient sensor in dynamic mixed-mode fracture mechanics experiments. J Mech Phys Solids 1992;40(3):641–61.
[9] Kiruguluge MS, Tippur HV. Mixed-mode dynamic crack growth in functionally graded glass-filled epoxy. Exp Mech 2006;46(2):269–81.
[10] Kirugulige MS, Tippur HV. Measurement of fracture parameters for a mixed-mode crack driven by stress waves using image correlation technique and high speed digital photography. Strain 2009;45(2):108–22.
[11] Periasamy C, Tippur HV. A full-field digital gradient sensing method for evaluating stress gradients in transparent solids. Appl Opt 2012;51 (12):2088–97.
[12] Periasamy C, Tippur HV. Measurement of crack-tip and punch-tip transient deformations and stress intensity factor using digital gradient sensing. Eng Fract Mech 2013;98:185–199.
[13] Miao C, Sundaram BM, Huang L, Tippur HV. Surface profile and stress field evaluation using digital gradient sensing method. Meas Sci Technol 2016;27 (9). p. 095203 (16pp).
[14] Nakano M, Kishida K, Yamauchi Y, Sogabe Y. Dynamic Fracture Initiation in brittle materials under combined mode I/II loading. Journal de Physique IV Colloque 1994;04(C8). p. C8-695-700.
[15] Butcher RJ, Rousseau CE, Tippur HV. A functionally graded particulate composite: preparation, measurements and failure analysis. Acta Mater 1998;47 (1):259–68.
[16] Sundaram BM, Tippur HV. Dynamic crack growth normal to an interface in bi-layered materials: an experimental study using digital gradient sensing technique. Exp Mech 2016;56(1):37–57.
[17] Periasamy C, Tippur HV. Measurement of orthogonal stress gradients due to impact load on a transparent sheet using digital gradient sensing method. Exp Mech 2013;53(1):97–111.
[18] Prautzsch H, Boehm W, Paluszny M. Bezier and B-spline techniques. Berlin Heidelberg New York: Springer-Verlag; 2002.
[19] Jajam KC, Tippur HV. Role of inclusion stiffness and interfacial strength on dynamic matrix crack growth: an experimental study. Int J Solids Struct 2012;49(12):1127–46.
[20] Sundaram BM, Tippur HV. Dynamics of crack penetration vs. branching at a weak interface: an experimental study. J Mech Phys Solids 2016;96:312–32.
[21] Li Y, Fantuzzi N, Tarnabene F. On mixed-mode crack initiation and direction in shafts: strain energy density factor and maximum tangential stress criteria. Eng Fract Mech 2013;109:273–89.
[22] Sun CT. Fracture mechanics. Waltham: Academic Press; 2012.
[23] Faye A, Parameswaran V, Basu S. Effect of notch-tip radius on dynamic brittle fracture of polycarbonate. Exp Mech 2016;56(6):1051–61.
[24] Ravi-Chandar K. Dynamic fracture. San Diego: Elsevier; 2004.
[25] Krautkramer J, Krautkramer H. Ultrasonic testing of materials. Berlin: Springer-Verlag; 1990. p. 13–14, 533–534.